Improving the Prediction of the 3 July 2019 Kaiyuan Tornadic Supercell and Embedded Tornado with Radar and Surface Data Assimilation

Haojia Li,[a,b,c] and Ming Xue[b]

[a] *Key Laboratory of Mesoscale Severe Weather/Ministry of Education and School of Atmospheric Sciences, Nanjing University, Nanjing, 210093, China*
[b] *Center for Analysis and Prediction of Storms and School of Meteorology, University of Oklahoma, Norman Oklahoma 73072, United States*
[c] *POWERCHINA HUADONG ENGINEERING CORPORATION, Hangzhou, 311100, China*

October 24, 2025

Corresponding author: Ming Xue, mxue@ou.edu

Key Points:

- The impact of assimilating dense surface observations on improving the simulated 3 July 2019 Kaiyuan tornadic supercell is investigated.
- Dense surface data assimilation helps to improve the intensity and structures of the supercell and cold pool in the analyses and forecasts, as well as the inflow conditions that support the strong supercell with near-surface rotation.
- A realistic tornado is explicitly simulated through a tornado-resolving simulation nested within the best-performing supercell simulation and the tornado structure and evolution are documented.

Keywords:

Data assimilation, Tornado, High-resolution numerical simulation, Large eddy simulation

ABSTRACT

The 3 July 2019 Kaiyuan City, Liaoning Province, tornadic supercell is simulated with the WRF model, using up to five levels of nested grids, with the innermost grid having a 50 m grid spacing. Reflectivity and radial velocity data from seven operational Doppler weather radars in different wavebands are assimilated together with dense automatic weather station (AWS) data using a 3DVAR data assimilation (DA) and cloud analysis system on the third-level 450-m grid with 5-minute cycles. Experiments assimilating surface data in a different number of cycles show that the analyses and forecasts are improved in terms of the intensity and structures of the simulated supercell and cold pool, compared to the one without assimilating surface data. The frequent assimilation of high-resolution surface data tends to produce spurious convection due to imbalances introduced, which has negative impact on the development of near-surface rotation. With surface data assimilated in more cycles, more convective available potential energy (CAPE) is introduced in the final analysis, and more intense supercell is predicted. A 50-m tornado-resolving simulation is conducted by nesting within the best-performing 450-m forecast. The simulation successfully captures the genesis and evolution of a tornado reaching EF2 intensity, through the one-cell, two-cell, and multi-vortex stages of development. The track, life cycle, and in-storm location of the simulated tornado agree well with observations.

PLAIN LANGUAGE SUMMARY

Tornadoes are one of the most difficult-to-predict phenomena in the atmosphere given its quite small spatial and temporal scales. Accurate initial condition is essential for the prediction of tornadoes by numerical models. Assimilating data from weather radars has been shown to very helpful in predicting tornadic storms but radars at a significant distance from the storms cannot observe the conditions near the ground. Radars do not observe the atmosphere outside the precipitation regions either. The present work utilizes high spatial- and temporal-resolution surface observations from automated weather stations, by assimilating them into a storm prediction model. The additional surface station observations improve the analyses and forecasts of the Kaiyuan tornadic supercell storm. A successful simulation of the embedded tornado is obtained when using a tornado-resolving 50 m grid. This represents the first time a real tornado in China is simulated through the assimilation of radar and surface station data.

1. Introduction

Severe convective storms, such as supercells, have high damaging potential around the world (Meng et al., 2016; Xue et al., 2016; Yokota et al., 2016; Meng et al., 2018; Luo et al., 2020; Zheng et al., 2020). With the desire to shift severe weather warnings from warn-on-detection to warn-on-forecast paradigm, accurate prediction of individual supercells and their associated tornadoes using numerical weather prediction (NWP) models becomes an essential step but remains a significant challenge (Stensrud et al., 2009; Stensrud et al., 2013; Sun et al., 2014). One major reason is the poor representation of the initial conditions for the storms within the NWP models and improving the initial conditions through advanced data assimilation is critically important.

In recent years, a number of studies have focused on improving tornadic supercell simulation/prediction through radar data assimilation (DA) (Xue et al., 2003; Hu et al., 2006a; Hu & Xue, 2007; Dawson et al., 2012; Jung et al., 2012; Xue et al., 2014; Yokota et al., 2016; Putnam et al., 2019; Snook et al., 2019). Compared with other observational instruments (such as surface weather stations), Doppler radars have higher spatial and temporal resolutions and are the only observational tool that can resolve internal storm-scale structures. However, considering the Earth's curvature and the elevation angle of the lowest radar beam (typically 0.5°), the lowest radar beam can be a few kilometers above the ground surface when the radar is located more than a hundred kilometers away. In such cases, the spatial coverage of the radar observations is incomplete at low levels. This would reduce the effectiveness of the radar data assimilation since the low-level rotational features of supercells are mostly within this region. Another factor to consider is that radar data are limited to the precipitation regions; they do not sample the storm environment or directly measure thermodynamic properties, including temperature and moisture. Combined assimilation of radar data together with conventional observations that sample the storm environment has the largest potential to improve convection storm prediction.

Over the past few decades, the proliferation and enhancement of surface observation networks, including the automatic weather stations (AWS), have led to a substantial increase in the availability of high-resolution surface observations (Brock et al., 1995; Fiebrich, 2009; Landolt et al., 2019). Within China, the AWS stations in many regions reach spaces of less than 10 km and temporal resolutions of less than 5 min (Zhang et al., 2020b). They have become invaluable for monitoring surface-based mesoscale and storm-scale features that are crucial for forecasting convective storms and their associated severe weather hazards. The

assimilation of such dense surface data is also expected to fill the low-level data voids of weather radars, in addition to providing direct in-situ measurements of temperature and moisture.

A number of studies have tried to improve the prediction of severe convective storms or systems via assimilating surface observations in addition to radar data (Zhang et al., 2004; Dong et al., 2011; Schenkman et al., 2011; Putnam et al., 2014; Snook et al., 2015; Yokota et al., 2016; Li et al., 2022). For example, Zhang et al. (2004) found within perfect-model observing system simulation experiments (OSSEs), an ensemble Kalman filter (EnKF) failed to produce an adequate analysis of a simulated supercell storm when the radar radial velocity data were only available above 4 km height. The analysis was much improved when surface station measurements of wind and temperature were also assimilated. Also employing the OSSE approach with EnKF DA, Dong et al. (2011) found that when the radar is far away from the main supercell storm so that the lowest few kilometers of the storm are not covered by the radar data, a clear positive impact of surface observations is achieved when the surface network spacing is less than 20 km. Schenkman et al. (2011) examined the impact of real X-band Doppler radar data and data from the Oklahoma Mesonet (Brock et al., 1995) on the prediction of a tornadic mesoscale convective system (MCS). They found that when the high-resolution observations from the close-distance X-band Doppler radars were absent (so that only more distant S-band radar data were available), assimilation of 5-min interval Mesonet observations (using a three-dimensional variational-cloud analysis DA system) had a significant positive impact on the analysis and forecast of tornadic mesovortices within the MCS. For the same MCS case but using EnKF DA, Snook et al. (2015) also found that the forecast of near-surface mesovortices within the MCS is substantially improved when surface observations are assimilated together with radar data. Later, Chen et al. (2016) showed that assimilating additional 5-min AWS observations using a four-dimensional variational (4DVAR) DA system could help improve the analysis and forecast of a squall line, especially at the low levels where radar data were lacking.

Despite the above studies, high spatial and temporal-resolution surface observations are still underutilized in operational NWP systems. Studies that evaluate the impact of surface and radar data assimilation on tornadic supercell prediction are even more limited. Yokota et al. (2016) is one of few such studies. They successfully simulated a strong low-level mesocyclone (LMC) near the path of an actual tornado with the assimilation of both surface and radar data. However, when either surface or radar data were removed, the LMC was no longer simulated. They also found that the low-level convergence ahead of the storm and the low-level relative

128 humidity (RH) in the rear of the storm were two key factors affecting the strength of the
129 predicted LMC.

130 The above cited studies assimilating real surface station and radar data were for United
131 States and Japan cases. The present study focuses on a tornadic supercell case that occurred in
132 Kaiyuan City, Liaoning Province, in northeastern China on July 3, 2019 (Zhang et al., 2020a;
133 Zheng et al., 2020). An EF-4-rated tornado struck the city in the afternoon of that day and
134 caused 7 fatalities and 190 injuries. In our previous study (Li et al., 2024), a high-resolution
135 numerical simulation was conducted to investigate the convective initiation mechanism of the
136 tornadic supercell at the initial stage, and the simulation started from an analysis of the Global
137 Forecast System (GFS) of NCEP without assimilating local data. The simulated supercell
138 exhibited significant discrepancies in terms of supercell storm intensity, structure, and
139 morphology when compared with the observed one. One major objective of this study is to
140 improve the simulation of that tornadic supercell by assimilating local surface and radar data.

141 There exist in the literature only a limited number of studies that attempt to simulate real
142 tornadoes or tornado-like vortices (TLV) from real initial conditions (Mashiko et al., 2009;
143 Schenkman et al., 2012; Xue et al., 2014; Mashiko, 2016; Mashiko & Niino, 2017; Snook et
144 al., 2019; Sun et al., 2019). With a 50-m grid spacing, Mashiko et al. (2009) were able to
145 simulate a tornado that occurred in the outer rainband of a landfalling typhoon; the
146 tornadogenesis processes were analyzed based on the simulation. Using a similar approach,
147 Mashiko (2016) and Mashiko and Niino (2017) simulated the Tsukuba City, Japan, supercell
148 tornado with a horizontal grid spacing of 10 m. With the assimilation of high-frequency radar
149 data, Xue et al. (2014) reproduced well the 8 May 2003 Oklahoma City tornadic supercell.
150 Their 50-m simulation captured two-cell and multi-vortex tornado structures that had only
151 previously been simulated by idealized simulations. More recently, Sun et al. (2019) simulated
152 an EF4 tornado that occurred on 23 June 2016, in Funing, Jiangsu Province, China, using a
153 multi-level nested 49-m grid spacing. The development of multi-vortex structures within the
154 simulated tornado is attributed to barotropic instability that excites vortex Rossby waves
155 (Huang & Xue, 2023). However, without assimilating local data, their simulated tornadic
156 supercell had large location and timing errors (Sun et al., 2019).

157 In this study, we try to improve the simulation of the tornadic supercell reported in Li et al.
158 (2024) by assimilating operational radar and high-density surface station data using a three-
159 dimensional variational (3DVAR) method on the 450-m nested grid. We then increase the grid
160 resolution by further nesting two grids of 150 m and 50 m grid spacings in an attempt to
161 explicitly predict the tornado or tornado-like vortex. The 3DVAR method is chosen because of

its much lower computational cost than EnKF, especially at the 450 m grid spacing; there are a number of prior examples using the 3DVar method for initializing tornadic supercell storms (Hu et al., 2006a; Hu et al., 2006b; Hu & Xue, 2007; Stensrud & Gao, 2010; Xue et al., 2014). To the best of the authors' knowledge, the current study represents the first time a real tornado in China is simulated through the assimilation of multi-radar data and dense surface station data.

The remainder of the paper is organized as follows. The tornadic case to be studied is first briefly introduced in section 2. The data to be used as well as the experiment design are described in section 3. Section 4 presents the analysis and forecast results on the 450-m grid and evaluates the impact of surface data assimilation on the analysis and forecast results. The tornado-resolving simulation results on the 50-m grid are also presented in section 4. A summary and discussion are provided in section 5.

2. Case overview

The synoptic patterns and mesoscale features in the afternoon of 3 July 2019 have been shown in Li et al. (2024). At 1400 LST (hereafter all times are in LST, which is 8 hours ahead of UTC), 3 July 2019, a slow-moving northeast China cold vortex (NCCV, Sun et al., 1994; Xie & Bueh, 2015; Fan et al., 2023) in the form of a cut-off low was present at 500 hPa over northeast China. There were two short-wave troughs extending southwestwards and southwards from the cold vortex center. At 850 hPa, a low circulation was underneath the 500 hPa cold vortex, with a trough line extending southwestward and right behind Kaiyuan City, where the tornado of interest later occurred. At Kaiyuan, strong northwesterly flows were at 500 hPa, while at 850 hPa the flow was southwesterly ahead of the trough, and the low-level southwesterly flow passed over the Bohai Bay to the south and was rich in moisture. The strong northwesterly upper-level flow overlaying the moisture-rich southwesterly low-level flow provided strong vertical wind shear and favorable conditions for rotating thunderstorms (see Fig. 1 of Li et al. (2024)).

As described in Li et al. (2024), the parent tornadic storm first appeared near the southwestern section of an MCS at 1638 LST and grew rapidly into a supercell in the next 30 minutes while moving southeastward to Kaiyuan (Zheng et al., 2020). At ~1715, the tornado occurred north of Kaiyuan City and moved southward along with the storm. The tornado dissipated at ~1747 (Zhang et al., 2020a). Based on a numerical simulation, Li et al. (2024) showed that the storm that later evolved into the tornadic supercell was triggered by gravity waves propagating along a stable but moist layer that acts as a wave guide above a boundary

layer, and the gravity waves were excited by intense convection within the MCS. Here, we first describe the evolution of the established Kaiyuan tornadic supercell based on radar observations (Figures 1 and 2).

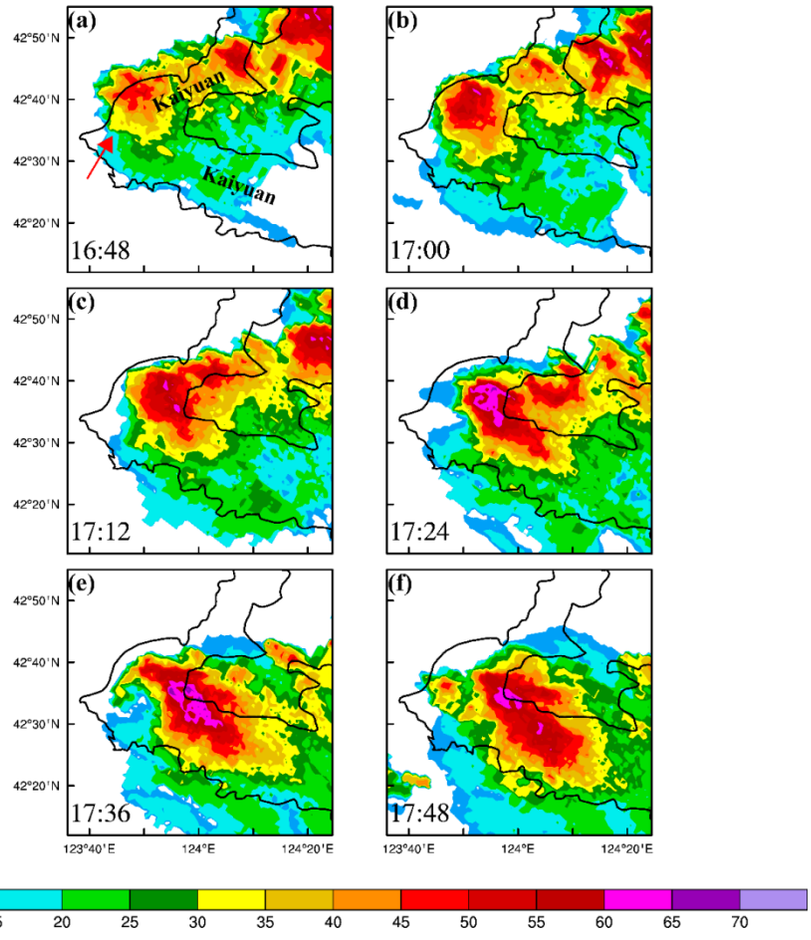

Figure 1. (a-l) Observed radar composite reflectivity (shaded) from 1648 to 1748 LST at 12-min time intervals. The bold black lines outline the boundary of Kaiyuan City, which occupies a C-shaped region. The red arrow in (a) points to the supercell of interest.

The tornadic supercell was captured by the Shenyang (SY) radar and other operational radars in the proximity (see Figure 3). After the initial cell of the supercell was triggered, it quickly grew into a deep convective storm (Figures 1a and 1b). By 1700 LST, the entire storm had moved into the boundary of Kaiyuan City (Figure 1b). During the next 20 minutes, the storm intensified quickly and generated a wider precipitation region (Figures 1c-d). A region with reflectivity exceeding 60 dBZ suggests the presence of hail within the storm (Figure 1d). After that, the storm remained over Kaiyuan City for about half an hour (Figures 1d-f). In the end, it propagated southeastward and entered its decaying stage after 1800 LST (not shown).

The low-level evolution of the tornadic storm can be illustrated by the radar reflectivity (Z) and radial velocity (V_r) at the 0.5° elevation angle from the Shenyang radar. At 1722 LST, a

clear hook echo has formed at the northwestern end of the storm. Meanwhile, an inbound-outbound radial velocity couplet is collocated with the hook echo on the V_r map, suggesting the presence of the tornado (Figures 2a and 2d). According to the field report, the Kaiyuan tornado had just formed at the time (Zhang et al., 2020a). After it was generated, the tornado was maintained for about 20 minutes before dissipating (Figures 2e-f and 2j-l), producing a surface damage track of about 14 km length (Zhang et al., 2020a). Additional details on this case can be found in Li et al. (2024) and Zheng et al. (2020).

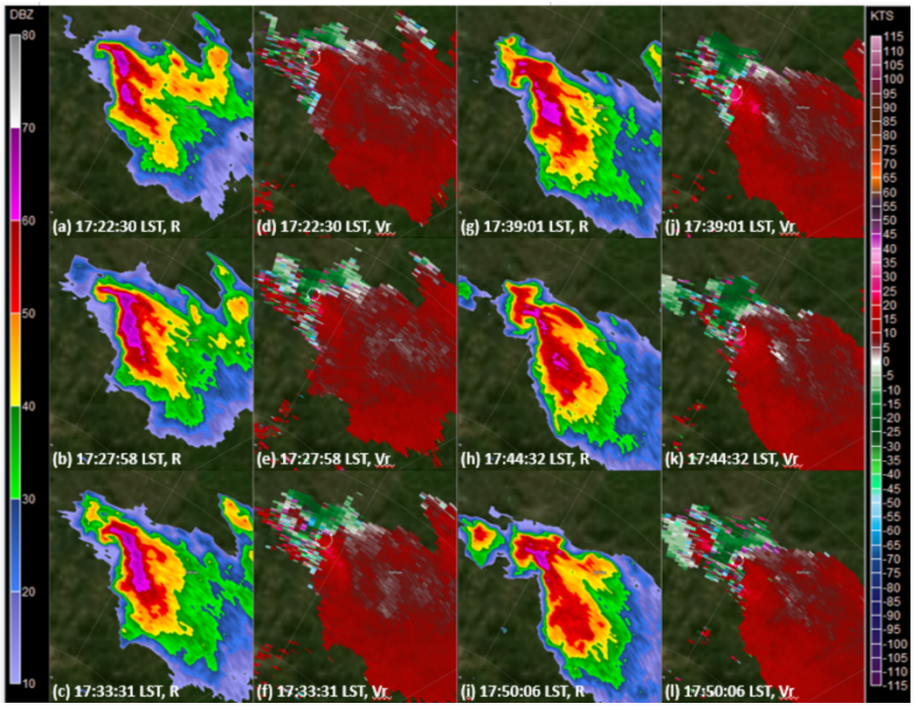

Figure 2. (a-c, g-i) Base radar reflectivity (shaded, dBZ) and (d-f, j-l) radial velocity (shaded, KTS) at the 0.5° elevation angle from the Shenyang radar at different times (LST) on July 3, 2019. The white circles denote the velocity couplets.

3. Data sets and experiment design

The fifth-generation ECMWF global reanalysis (ERA5) data (Hersbach et al., 2020) are used to provide the initial condition to spin up the initial background forecast, and to provide boundary conditions at hourly intervals for the outermost D1 grid. The advanced research version of the Weather Research and Forecasting (WRF-ARW) model version 3.9.1 (Skamarock et al., 2008) is used to perform simulations for all experiments. As in Li et al. (2024), three two-way nested domains, D1, D2, and D3, with the same coverages and the same set of physical parameterization schemes, are used first, except for the configuration of vertical

model levels. To better capture the low-level rotational features of the supercell, five more levels are added within the lowest 1 km above ground. Therefore, all grids have 56 vertical levels with spacing that stretches from about 20 m near the surface to 650 m at the model top. The D1, D2, and D3 domains have horizontal grid spacings of 4050, 1350, and 450 m, respectively. The outermost D1 domain spans the entire continental China, while the inner domains D2 and D3 cover the northeastern China and the region of active mesoscale convection, respectively (see Fig. 4 of Li et al. (2024) for the grid configuration). Figure 3 shows domain D3, together with two additional one-way nested grids, D4 and D5, added at later times (see more information later). As described in Li et al. (2024), the model used Morrison two-moment microphysical scheme (Morrison & Grabowski, 2008), Pleim–Xiu land surface and surface layer models (Pleim, 2006), the Asymmetric Convective Model, version 2 PBL scheme (Pleim, 2007), and the Community Atmosphere Model, version 3 radiation schemes (Collins et al., 2004) on all domains. None of these grids used cumulus parameterizations. A simulation is first run with the three nested grids from ERA5 analysis at 0000 UTC (0800 LST), 3 July 2019, through 0900 UTC when the DA cycles start.

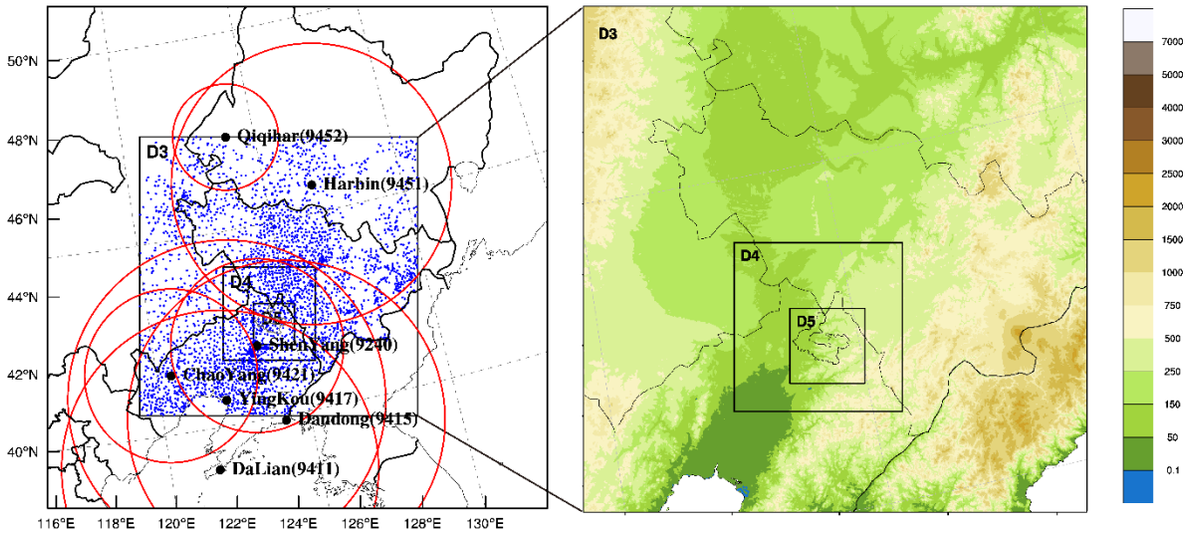

Figure 3. (left) The D3 model domain (green rectangular box) and locations of the radar stations (large black dots) and dense AWSs (small blue dots). There are seven radars, including Qiqihar (9452), Harbin (9451), Shenyang (9240), Chaoyang (9421), Yingkou (9417), Dandong (9415), and Dalian (9411) radar, used to cover the entire D3 domain. The maximum range of each radar is shown by the red circles. An enlarged view of the D3 domain (of 450 m grid spacing), including terrain elevation (shaded) and the nested D4 and D5 domains (of 150 and 50 m grid spacings), is shown on the right. The coverages of the outer domains D1 and D2 are not shown but can be found in Li et al. (2024).

The dense surface data, including station pressure, temperature, dew point, wind speed, and wind direction, from 3356 AWSs with high spatial (<10 km) and temporal (~5 min) resolutions, and radar base data from China New Generation Weather Radar (CINRAD) network are assimilated on the 450-m grid (Figure 3). The CINRAD network consists of more than 200 radars in total (Zou et al., 2018), and seven of them (see the radar locations in Figure 3), operating at S band and C band and manufactured by three different companies, are included to cover the D3 domain. Before DA, the reflectivity and radial velocity data are first quality controlled, with the procedure including despeckling, ground clutter and anomalous propagation artifact removal, and velocity dealiasing. The quality-controlled data are then checked by visual inspections and further adjustments are made. In the end, the data from the radar coordinates are interpolated to the WRF model grid for assimilation. For the dense surface data, a spatial-temporal continuity check is made before they are assimilated. In this procedure, data that have large differences from surrounding stations or previous or next observation times are excluded.

The Advanced Regional Prediction System (ARPS) three-dimensional variational (3DVar) data assimilation and cloud analysis system (Gao et al., 1999; Gao et al., 2004; Hu et al., 2006a; Hu et al., 2006b; Gao & Stensrud, 2012; Gao et al., 2013) suitable for convective-scale DA is used to assimilate the observations discussed earlier. The ARPS 3DVAR uses an incremental form of the cost function that includes the background, observation, and mass-continuity equation constraint terms. The analysis variables include three wind components (u, v, and w), potential temperature (θ), pressure (p), water vapor mixing ratio (q_v), and hydrometeor mixing ratios of cloud water (q_c), cloud ice (q_i), rainwater (q_r), snow (q_s), and hail (q_h). The mass continuity equation is used as a weak constraint in the 3DVar cost function to link the three wind components together for them to satisfy mass continuity, and temperature and moisture within cloudy regions are adjusted in cloud analysis based on the moist-adiabatic method as described in Hu et al. (2006a). Additional details on the reflectivity observation operator used can be found in Chen et al. (2020).

Given that we are dealing with different observation types sampling very different spatial scales, multiple analysis passes are performed, with each pass including different data types using different spatial error decorrelation scales. The use of multiple passes assimilating different types of data has been a standard practice with the ARPS data assimilation system (e.g., Xue & Martin, 2006; Liu & Xue, 2008; Schenkman et al., 2011). The selection of the decorrelation scales is guided by the mean density of observational data assimilated. In our case, three analysis passes are used. The surface data are analyzed in the first pass with

horizontal and vertical influence radii of 20 and 0.5 km, respectively, while the radar radial velocity are analyzed in the second pass, and the reflectivity are analyzed in the third pass, respectively, with both using horizontal and vertical influence radii of 2 grid points.

Four experiments are designed to investigate the impact of DA on the analysis and forecast of the supercell (Figure 4). The experiments mainly differ in the number of surface DA cycles performed. Since the duration from supercell initiation to tornadogenesis is relatively short (only about 30 minutes), limited radar observations are available to build up the supercell in the model through radar DA. Therefore, the DA window starts at 1700 LST and ends at 1730 LST, which actually overlaps with the tornadogenesis time at 1717 LST.

The DA is performed on the 450-m D3 grid only for all four experiments. At 1700 LST, simulations on the nested D1-D3 grid are run to the time when observations are first assimilated in each corresponding experiment. The first DA experiment, 1C_sfc, assimilates surface and radar data in a single DA cycle, at 1730 LST. The other three experiments assimilate radar data every 5 minutes starting from 1705 LST through 1730 LST. Experiment no_sfc assimilates radar data only without surface data, while experiment allC_sfc assimilates both radar and surface observations in all cycles. Experiment last2C_sfc assimilates surface data only in the last two cycles. When the DA window ends at 1730 LST, a 2-hour simulation is produced from the final analysis of each experiment on the three nested grids, and the results of the 450-m grid are discussed in section 4. We note here that even though DA is only performed on the 450-m grid, because the grid nesting is two-way interactive, the model initial conditions within the region covered by the 450-m grid are effectively those of the 450-m grid, albeit at reduced resolutions.

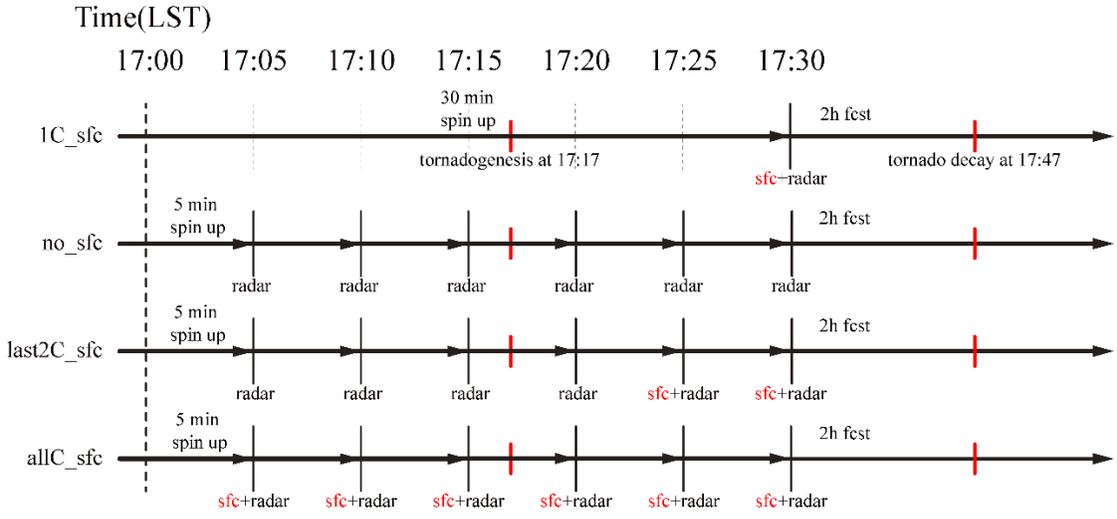

Figure 4. Illustration of data assimilation and forecast cycles for four experiments. 'sfc' represents the surface data from AWSs, 'radar' represents the radar data, including radar radial velocity and reflectivity. The black solid vertical lines indicate the times at which observations are assimilated. The red vertical lines indicate the times of tornadogenesis and tornado decay.

To see if a tornado or a tornado-like vortex similar to the Kaiyuan tornado can be obtained in the simulation given enough resolution, we further nest two one-way-interactive grids, D4 and D5, with horizontal grid spacings of 150 m and 50 m, respectively, within the D3 domain (see right panel of Figure 3). D4 domain (150-m grid spacing) is initialized from the interpolated D3 domain (450-m grid spacing) at 1814 LST. The D5 (50-m grid spacing) domain is interpolated from the D4 domain and starts at 1824 LST. The 10-minute time lag between D4 and D5 provides spin-up time for the intensification of the near-surface rotation in D5 and is found to be the best-performing configuration among a set of experiments with different starting times of the forecast (not shown).

4. Analysis and forecast results

4.1 Innovation statistics of analyses and forecasts

To quantify model analysis and forecast quality and compare the performance of different experiments, the root-mean squared innovations (RMSIs) of the simulated radial velocity and reflectivity against radar observations are calculated over a 30 km × 30 km region roughly centered on the observed and simulated supercell storms. The RMSIs of analysis and forecast

results against surface observations, including station pressure, temperature, dew point, wind speed, and *u* and *v* components of surface wind, are also calculated to show the effects of surface observation assimilation.

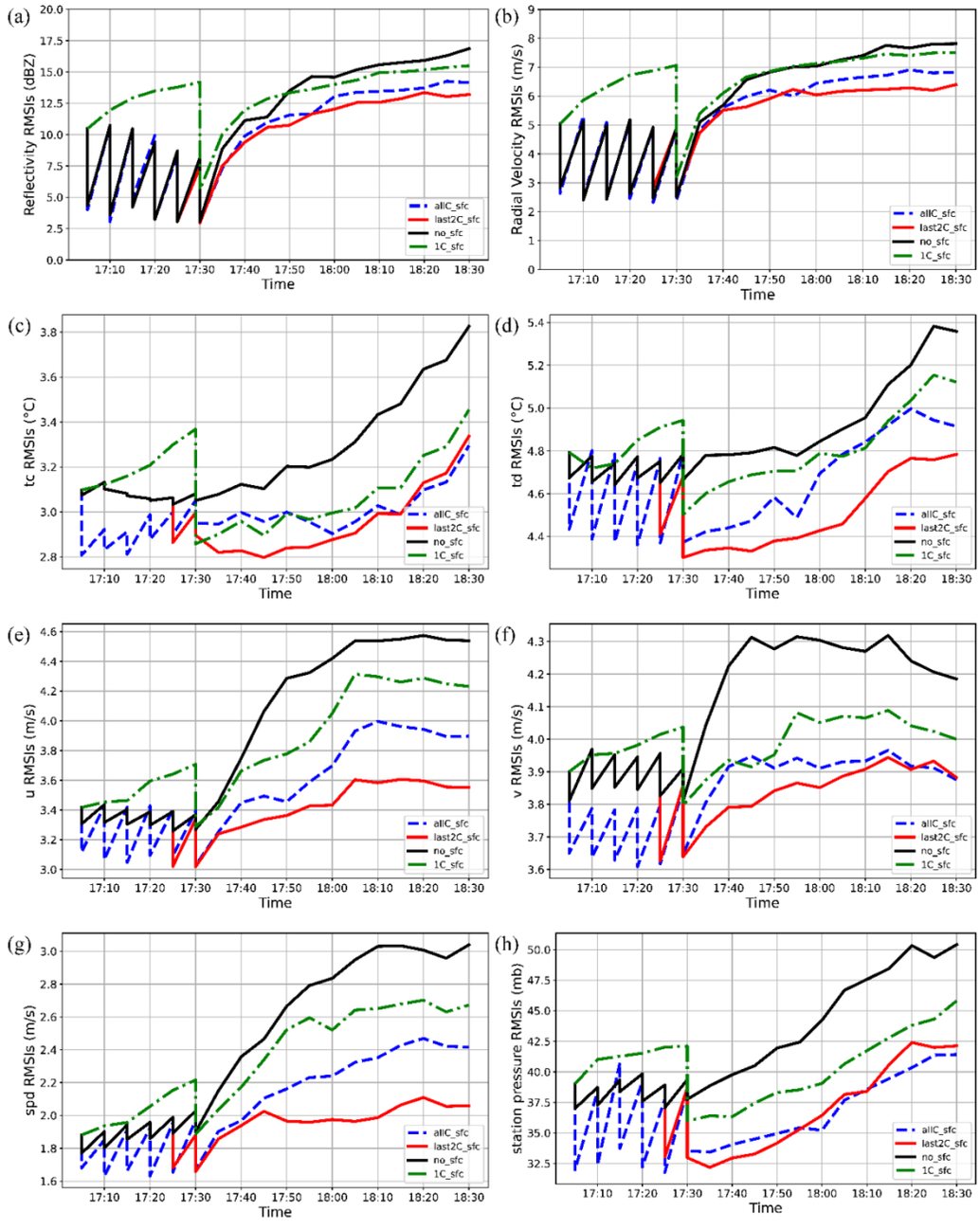

Figure 5. The RMSIs of reflectivity (a) and radial velocity (b) analyses and forecasts of four experiments against the 0.5° tilt of Shenyang radar observations. (c)-(h) The RMSIs of the analyses and forecasts of surface temperature, dew point temperature, u component of surface wind, *v* component of surface wind, wind speed, and station pressure, respectively, calculated against surface station measurements.

Figures 5a and 5b show the RMSIs of reflectivity and radial velocity analyses and forecasts from the four experiments. During the DA cycles, experiments no_sfc and allC_sfc exhibit similar errors in analyzed radial velocity and reflectivity, suggesting that the additional surface DA has a limited influence on the internal structures of simulated storms. Experiment last2C_sfc experiences identical assimilation cycles as no_sfc until the last two cycles, therefore, it has the same RMSIs as the latter in the first five cycles. Not surprisingly, with only one cycle DA at the end, the errors of 1C_sfc increase quickly at the beginning and are higher than those of the other three experiments at the final analysis time. They are also the highest during the first 20 minutes of forecast. In no_sfc, without the help of surface DA, the RMSIs of the forecasts grow faster than allC_sfc and last2C_sfc, especially at the beginning of forecast. Its errors reach and exceed those of 1C_sfc after 20 minutes and remain the highest through the end of 2-hour forecast.

Figures 5c to 5h show the RMSIs of analyses and forecasts against surface observations during the DA cycles and for the ensuing period. The RMSI of surface temperature in 1C_sfc (Figure 5c) increases quickly before DA is performed. When only radar data are assimilated at the start, the RMSIs of surface temperature are reduced slightly after each assimilation cycle in no_sfc. However, when additional surface data are assimilated, the RMSIs of surface temperature are significantly reduced (Figure 5c, see the RMSI drop after each surface DA in allC_sfc, last2C_sfc, and 1C_sfc). During the forecast period, the errors in all experiments grow over time, only the ones in last2C_sfc decrease briefly before rising. The RMSIs of remaining variables (Figure 5d-h) show similar patterns as surface temperature, only the amplitudes of “saw tooth” during the DA window and hence the forecast error growth rates vary.

Generally, the RMSIs from allC_sfc and last2C_sfc are lower during the DA window and subsequent forecast. In contrast, errors in no_sfc are the highest at the end of the DA window and remain the highest during the forecast. The faster error growth in no_sfc compared to the other experiments indicates that the low-level conditions improved by the surface observations underneath the storm and in the immediate environment of the storm are beneficial to the storm prediction. Although only one cycle of surface DA is performed in 1C_sfc, the errors are significantly reduced and are lower than those of no_sfc at the final analysis time and remain lower during the subsequent forecasts, again shows the benefits of surface DA.

4.2 Analysis fields on the 450-m grid

In this section, analyses of the four experiments are verified against the observations from SY radar. The model radar reflectivity and radial velocity are simulated from the gridded analysis fields and projected onto the 0.5° elevation angle of SY radar (Figures 6 and 7). At a distance of about 100 km from the radar (see Figure 3), the 0.5° elevation is about 1 km above ground. A polarimetric radar data simulator developed by the Center for Analysis and Prediction of Storms with support for various microphysics schemes is used (Jung et al., 2008; Jung et al., 2010). Here, simple geometric mapping and spatial interpolation are used to simulate the radar observations. Beam pattern weighting or reflectivity weighting for radial velocity simulation is not included for simplicity.

At the time of final analysis, the observed tornado had formed and the observed supercell had entered its mature stage (Figures 6a and 7a). For the storm morphology, a well-defined hook echo existed at its northwestern end. The general forward flank precipitation region was located to the southeast of the hook echo, suggesting strong northwesterly winds at high levels. Meanwhile, a noticeable inbound-outbound radial velocity couplet near the hook echo at the northwestern end of the storm indicates the existence of a strong LMC (see the black arrows in Figure 7a).

The simulated radar reflectivity from each experiment shows a general agreement with the observations. Specifically, the morphology of the simulated storms in all experiments, including the position of the hook echo and the forward flank precipitation region, agrees well with the observed one. However, the intensity of the simulated storm in 1C_sfc is relatively weak (Fig. 6b) compared with the observed one. In contrast, the storms in other multi-cycle experiments exhibit stronger intensity, which is more consistent with the observed storm. This can be attributed to just one radar DA cycle in 1C_sfc which appears insufficient. Another clear deficiency is seen in no_sfc, in which spurious weak echoes are found to the west of the simulated supercell (Figure 6c). Fortunately, these echoes remain weak during the DA cycles and dissipate quickly in the subsequent forecast (see later). In terms of the simulated radial velocity fields, all experiments successfully reproduce the velocity couplets near the northwestern tips of the supercells (as denoted by the white circles in Figures 7b-e). Given that radar data are assimilated at this time of analysis, the agreements between analyzed and observed variables are not unexpected.

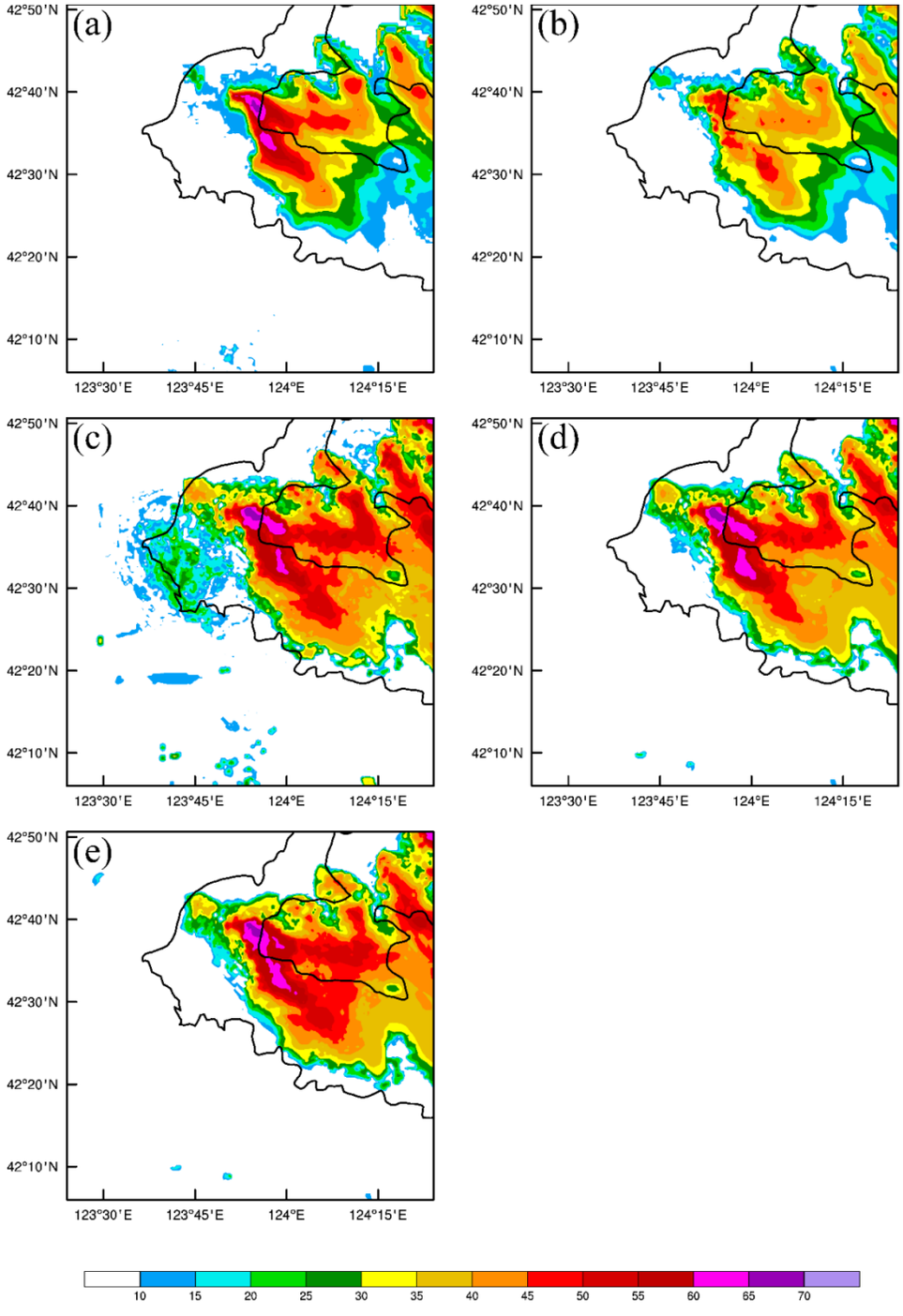

Figure 6. (a) The observed reflectivity (dBZ) fields at 1730 LST from the SY radar at 0.5° elevation. (b)-(e) Corresponding reflectivity fields from the 1730 LST 1C_sfc, no_sfc, last2C_sfc, and allC_sfc analysis, respectively, remapped onto the radar 0.5° elevation. The black lines outline the borders of Kaiyuan City.

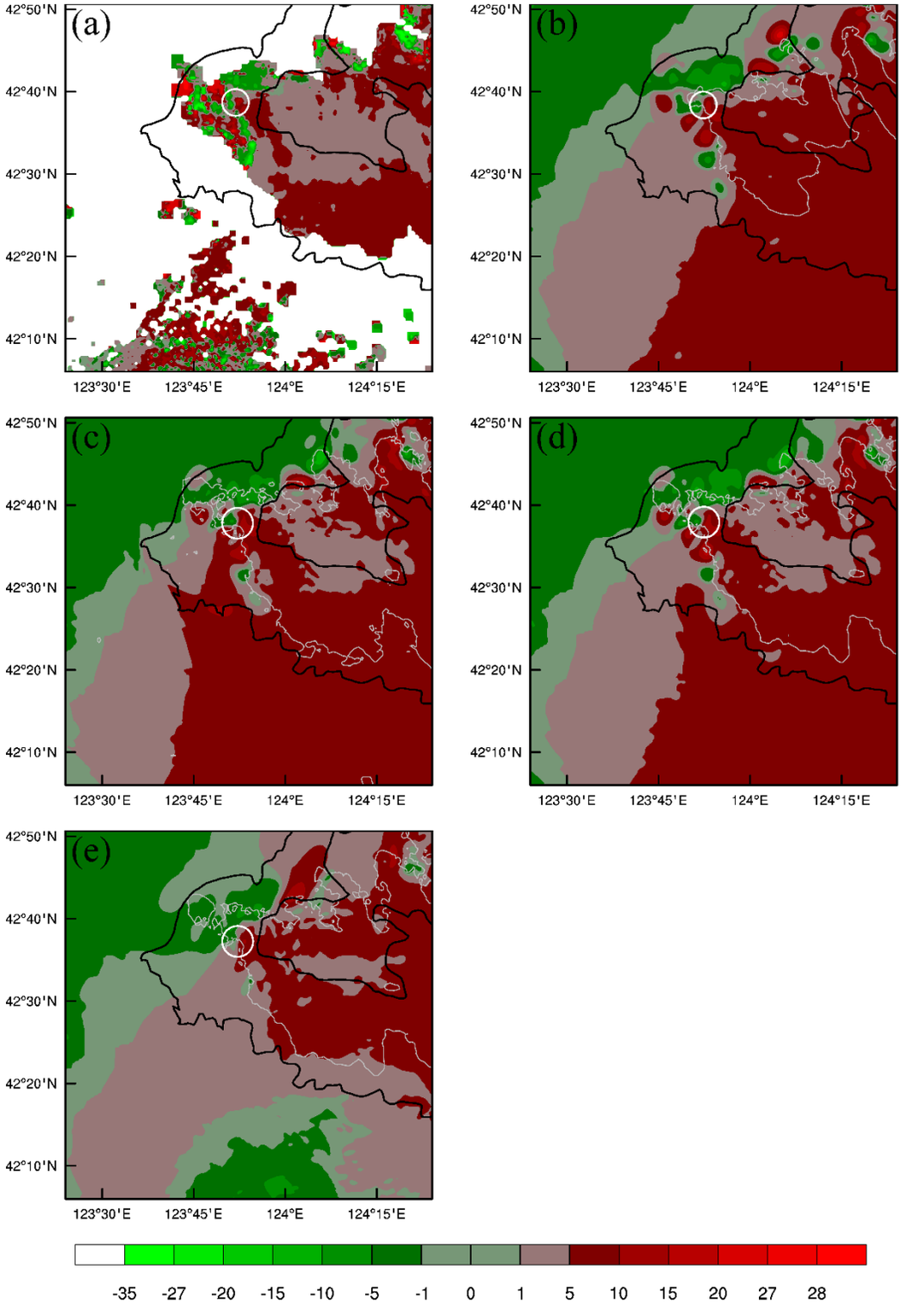

Figure 7. As in Figure 6, but for radar radial velocity (m s^{-1}) fields. The white contours outline the 30 dBZ reflectivity and denote the locations of the simulated storms. The white circles denote the location of LMC. The radar is located southwest of the displayed area.

In the simulation of Li et al. (2024) that was initialized from a global model analysis without assimilating any local data, significant discrepancy in the morphology and structure between simulated and observed supercells is attributed to possibly the poor representation of the simulated cold pool. To examine the simulated cold pool after DA, perturbation potential temperature fields from the final analyses of the four experiments are shown in Figure 8. The structure and intensity of the cold pools are significantly impacted by the DA (Figure 8). Specifically, the cold pool is more centered around the supercell rather than widespread ahead of the preceding MCS as in Li et al. (2024, see their Figure 7). In addition, without assimilating surface data, the storm in no_sfc generates a cold pool with detailed structure while its coverage is limited to the precipitation regions, because this cold pool is purely generated by the simulated storms (Figure 8a). In contrast, the cold pool in 1C_sfc is more diffuse and covers the wide rear flank precipitation region (Figure 8d). This is because in 1C_sfc, the hydrometeor species introduced by the cloud analysis at the final analysis time has not had a chance to produce evaporative cooling to enhance the cold pool yet, while the assimilated surface observations directly help establish the cold pool, though the pattern tends to be smooth due to limited spatial resolution. The cold pools in allC_sfc and last2C_sfc are in-between those of no_sfc and 1C_sfc. They both have the detailed cold pool structures seen in no_sfc and the weaker cold pool behind rear flank gust front (in this case, the north portion of the storm) as in 1C_sfc. Compared to no_sfc and 1C_sfc, allC_sfc and last2C_sfc also exhibit better-constructed gust fronts and stronger near-surface vortices at the leading edge of the gust front (Figures 8b and 8c), suggesting a higher potential for tornado formation in their subsequent forecasts.

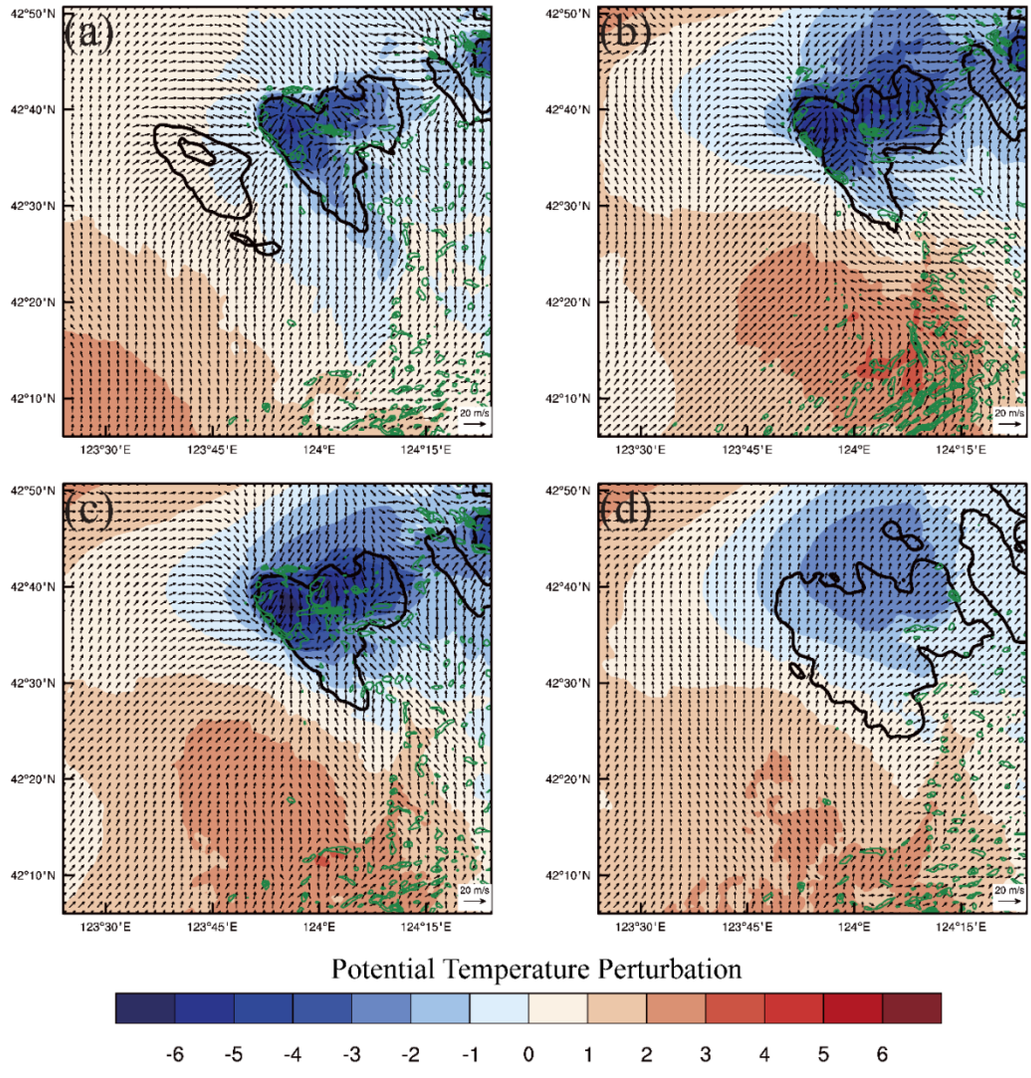

446

447 **Figure 8.** Perturbation potential temperature (shading, K), horizontal wind vectors
448 (m s^{-1}), and vertical vorticity (solid green contours in increments of 0.001 s^{-1}
449 starting at 0.001 s^{-1}) fields at the first model level above ground of the final analyses
450 at 1730 LST for (a) no_sfc, (b) allC_sfc, (c) last2C_sfc, and (d) 1C_sfc. The heavy
451 black contours in (a)-(c) denote the boundary of 30-dBZ reflectivity at the first
452 model level, but for 30-dBZ composite reflectivity in (d).

453

454 The above results have shown that the assimilation of radar reflectivity and radial velocity
455 data enabled reasonable construction of the tornadic supercell and associated vortex
456 circulations in the final analyses in all DA experiments. When assimilating additional surface
457 observations, experiments allC_sfc and last2C_sfc produce physically more consistent near-
458 surface features such as the cold pools. Such results are consistent with those of Schenkman et
459 al. (2011). In their study, the assimilation of 5-min observations from the Oklahoma Mesonet
460 had a substantial positive impact on the analysis and forecast of mesovortices, and the impact

was comparable to that of low-level radial velocity data from a dense X-band radar network. Chen et al. (2016) also found that low-level features of a squall line, including cold pool, gust front, and low-level winds, are improved after assimilating dense surface data. In the following section, we will further examine the impact of DA on short-range forecasts.

4.3 Forecasts on the 450-m grid

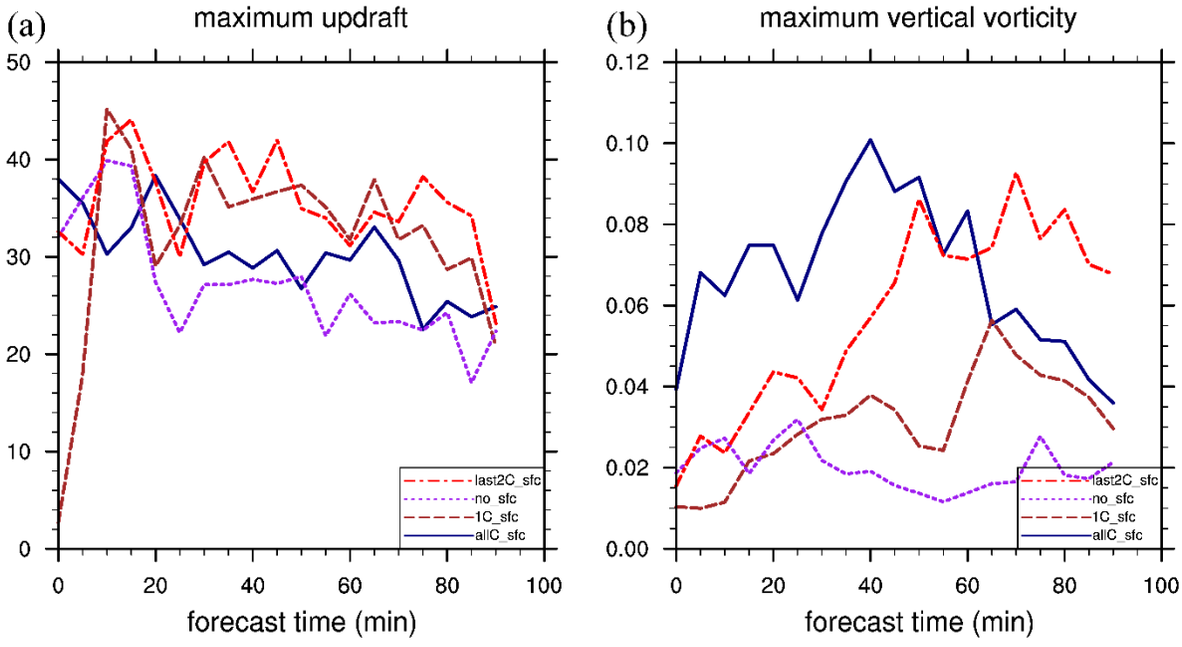

Figure 9. (a) Maximum updraft (m s^{-1}) at mid-levels (3-6 km) and (b) maximum near-surface vertical vorticity (s^{-1}) within the predicted supercells during the first 90 minutes of forecasts for experiments 1C_sfc, no_sfc, last2C_sfc, and allC_sfc.

In this section, we present the forecast results starting from the final analyses of four experiments at 1730 LST. Figure 9 shows the general evolution of the simulated supercell in terms of the time series of maximum mid-level updraft speed and the maximum near-surface vertical vorticity ζ. In the three experiments that assimilate radar data in multiple cycles, the supercells achieve strong updrafts exceeding 30 m s^{-1} at the beginning of forecast. Experiment 1C_sfc lacks a strong updraft at the beginning (Figure 9a), but it intensifies quickly during the first 10 minutes of forecast. In the subsequent forecasts, the updraft strength in all experiments drops gradually but is maintained over 30 m s^{-1} most of the time. Among all experiments, the weakest and strongest updrafts during most of the forecast period are from no_sfc and last2C_sfc, respectively, suggesting the important role of surface data.

Similar to the maximum updraft speed, 1C_sfc produces the weakest near-surface ζ in the final analysis, due to clearly the lack of spin time after DA. Experiment allC_sfc produces the strongest ζ in the final analysis, apparently benefiting from the most amount of data assimilated (Figure 9b). In the subsequent forecast, the near-surface ζ in experiments that assimilate additional surface data increases gradually, but that in no_sfc remains small. Compared to the vorticity in allC_sfc and last2C_sfc, the one in 1C_sfc is much weaker but is stronger than that in no_sfc most of the time. The near-surface vorticity in allC_sfc increases quickly and achieves its maximum strength at about 40 minutes before decreasing and falling below that of last2C_sfc. The peak vorticity in last2C_sfc is reached at 70 minutes and the peak value is slightly below that of allC_sfc but the large value is maintained for longer (Figure 9b). The evolution will be further examined in terms of emulated radar observations later.

The predicted reflectivity and wind fields are projected to the 0.5° elevation of the SY radar and compared directly against radar observations at the 60-minute forecasting time (Figures 10 and 11). At this time, the real-world tornado had vanished, but the observed supercell is still strong and exhibiting supercellular structures, as indicated by a well-defined hook echo (Figure 10a) and a strong LMC (see the white circles in Figure 11a). Meanwhile, the simulated supercells in the experiments assimilating additional surface data are developing vigorously and demonstrating similar supercellular structures as well (Figures 10b, 10d, 10e, 11b, 11d, and 11e). Without surface DA, the simulated supercell in no_sfc exhibits a less-organized hook echo (Figure 10c) and a much weaker LMC (Figure 11c). In general, the evolution of the predicted supercells from the radar perspective is consistent with our previous time series results (Figure 9). Although the simulated supercell moves further southeastward and develops wider stratiform precipitation regions compared to the observed one, the direction of the cloud anvil and storm-relative position of the hook echo agree with the observation well. Clearly, the delay in the development of strong rotation in the forecast is a significant timing error. The relatively fast development of tornado within the real-world supercell storm, and the time it takes for assimilated radar and surface data to spin up and achieve significant impact on the simulated storm may be some of the reasons. Forecast model errors and errors in the environmental background and in the analyzed storm-scale structures can also contribute to the overall forecast error. Similar timing and position errors in forecast had also been noticed in a number of previous studies, such as in the tornado-resolving ensemble simulations of Snook et al. (2019), which showed substantial tornado track differences among the ensemble members initialized from EnKF ensemble analyses.

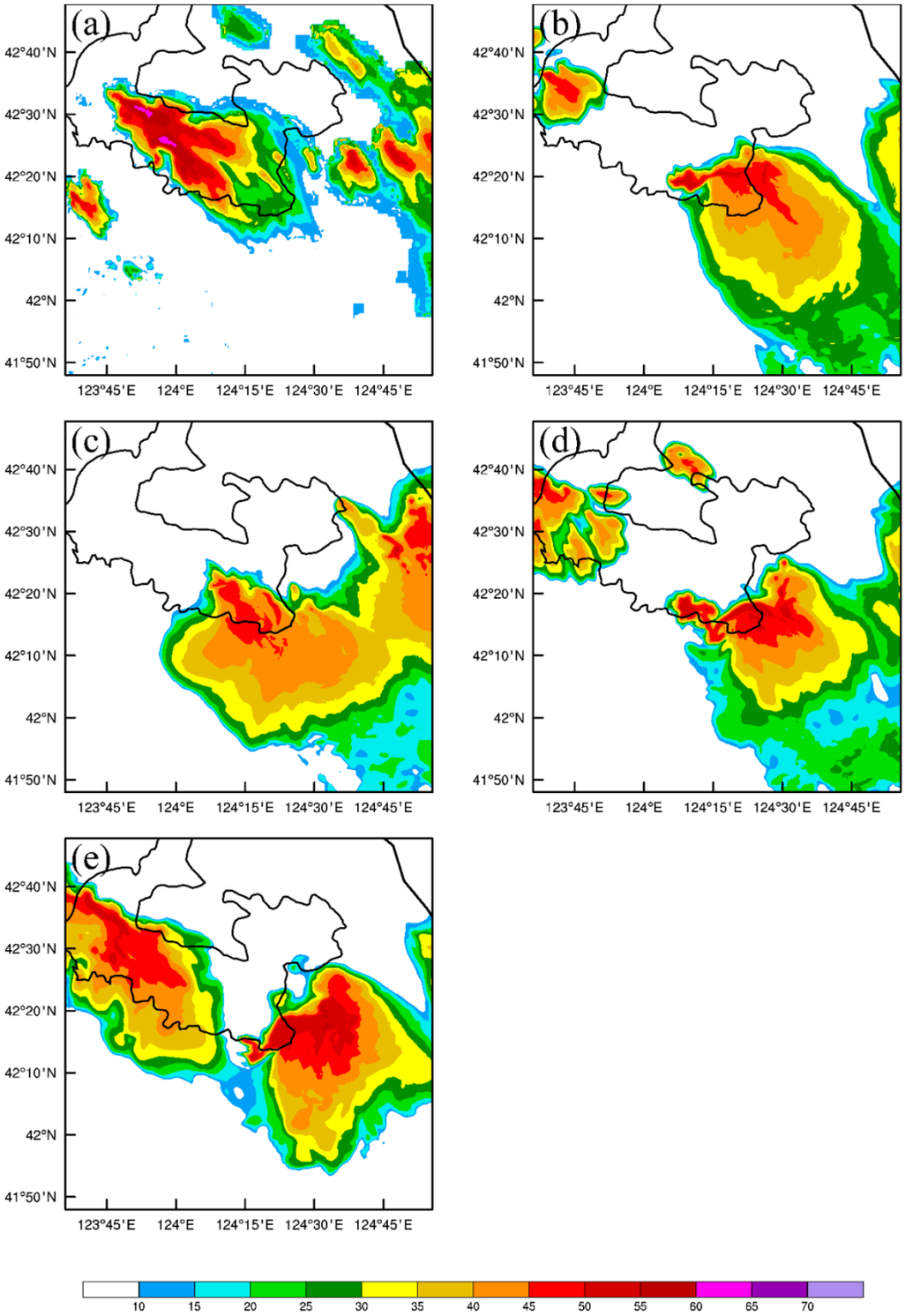

514

515 **Figure 10.** (a) The observed reflectivity (dBZ) fields at 1830 LST from the SY
516 radar at 0.5° elevation. (b)-(e) Predicted reflectivity fields from experiments
517 1C_sfc, no_sfc, last2C_sfc, and allC_sfc, respectively, remapped onto the radar
518 0.5° elevation at 1830 LST. The black lines outline the borders of Kaiyuan City.

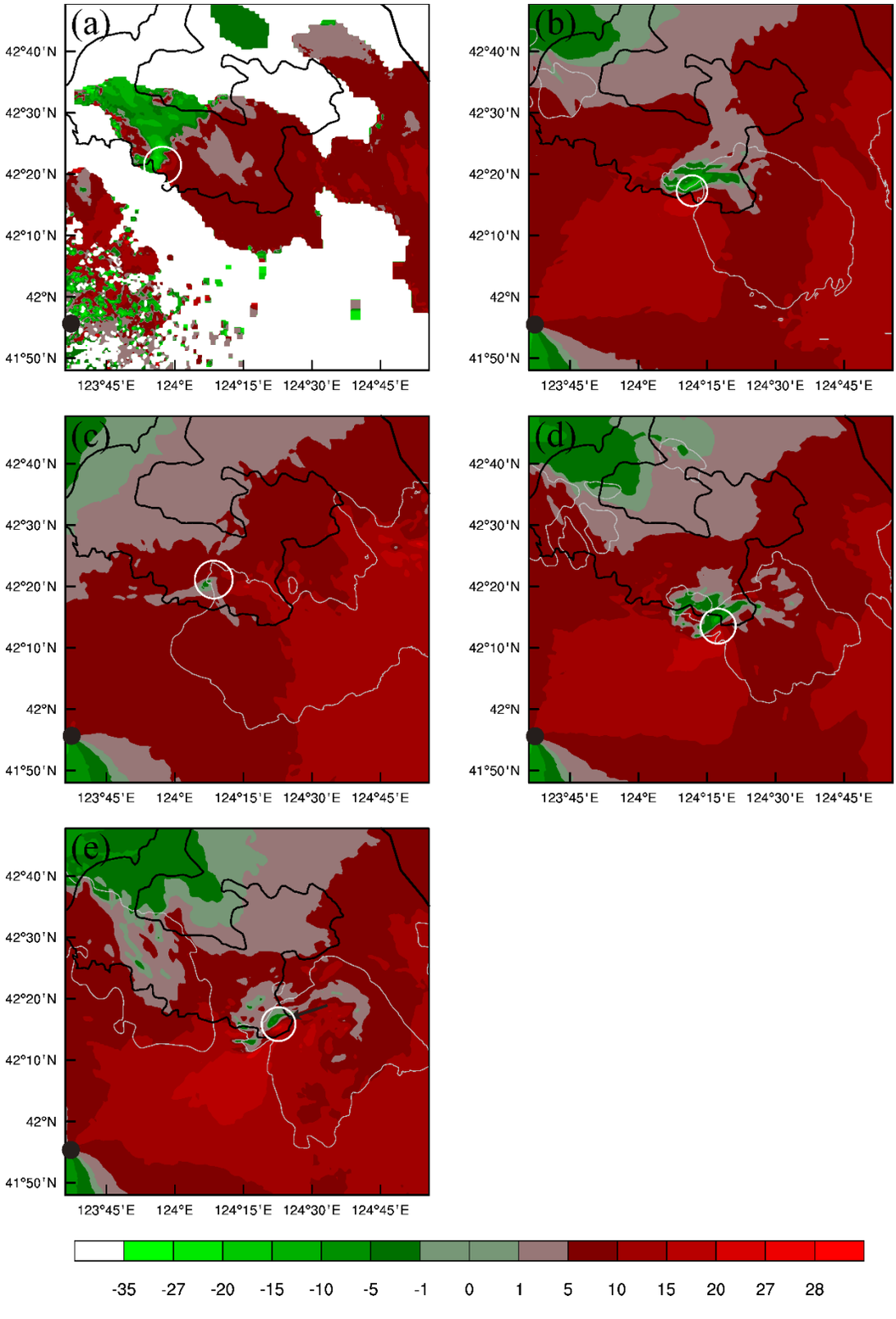

Figure 11. As in Figure 10, but for radar radial velocity (m s^{-1}) fields. The white contours outline the 30 dBZ reflectivity and denote the locations of the simulated storms. The white circles denote the locations of LMCs. The black dots denote the location of SY radar.

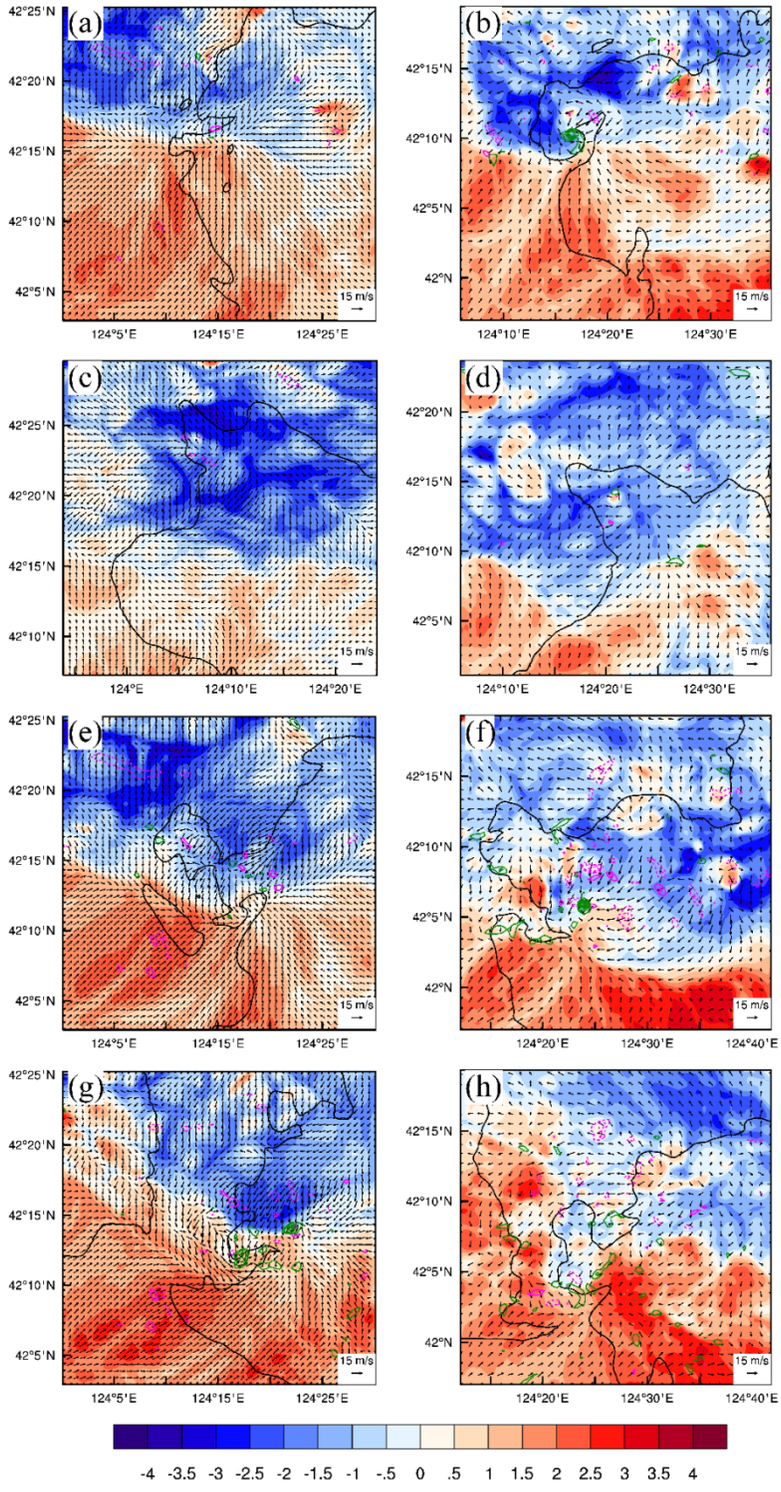

Figure 12. Perturbation potential temperature (shading, K), horizontal wind vectors (m s^{-1}), 30-dBZ reflectivity (thick black contours), w [solid (dashed) magenta contours in increments of 0.4 m s^{-1} starting at 1.6 (-1.6) m s^{-1}], and ζ (green contours in increments of 0.001 s^{-1} starting at 0.001 s^{-1}) at the first model level above ground at (left) 1820 and (right) 1845 LST for (a),(b) 1C_sfc, (c),(d) no_sfc, (e),(f) last2C_sfc, and (g),(h) 1C_sfc.

Previously, Figure 9b shows that the intensity of the near-surface vortex in allC_sfc decreases significantly shortly after it reaches maximum. Taking a closer look at the reflectivity fields in allC_sfc, spurious convection is found to be generated west of the simulated supercell (Figure 10e), which may be responsible for the weakening of the near-surface vortex in allC_sfc. To investigate the evolution of near-surface vortices further, the perturbation potential temperature θ', ζ and w fields at the first model level above ground are plotted in Figure 12.

It can be seen that the near-surface vortex first develops in allC_sfc near the hook echo of the supercell (Figure 12g), but it vanishes soon during the next 25 minutes (Figure 12h). In comparison, the near-surface vortex in 1C_sfc develops more slowly (Figures 12a and 12b), given its relatively weak parent storm (Figure 9). In last2C_sfc, the near-surface vortex develops 10 minutes later than that in allC_sfc but maintains for a longer period (Figures 12e and 12f). No near-surface vortex develops during the entire forecast of no_sfc (Figures 12c and 12d). Similar results were found in Yokota et al. (2016); when no surface data were assimilated, LMC did not develop in their forecasts.

Studies have shown that stronger and longer-lived (weaker or nonexistent) TLVs are often associated with a weaker (stronger) cold outflow (Snook & Xue, 2008; Marquis et al., 2012; Markowski & Richardson, 2014; Dawson et al., 2015). More specifically, the evaporatively cooled air that originated in the storm downdraft can be treated as a negatively buoyant source that has a negative impact on tornadogenesis when ingested into the tornado. Too strong cold pool can also cause misalignment between the low-level gust front forcing and the mesocyclone above (Snook & Xue, 2008). This is the case in no_sfc. The cold outflow produced by the supercell appears to be too strong to produce and maintain the near-surface vortex (Figure 12c). Consequently, no near-surface vortex forms during the subsequent forecast (Figure 12d). In contrast, with additional surface DA, the cold pool strength in the forecasts of all three other experiments is reduced to a moderate level, and the near-surface vortices are generated successfully at some point.

In allC_sfc, spurious convection continues to grow when the supercell develops and extends its southern part into the inflow region (Figures 12g and 12h), which has a negative impact on the development of the near-surface vortex. In contrast, the near-surface vortex in last2C_sfc develops under an undisturbed inflow environment, and is able to maintain for a longer period than that in allC_sfc.

We note that although 3DVAR is practical for high-resolution numerical simulation, it usually generates less dynamically balanced analysis fields for the lack of flow-dependent

forecast error covariance, in particular the cross-covariance among model state variables. Studies have shown that 3DVAR could produce spurious precipitation and large position errors of precipitation in the forecast (Hu & Xue, 2007; Vendrasco et al., 2016; Federico et al., 2019). These problems may worsen in a rapid-cycled DA framework. When dense surface data are assimilated in a 5-min interval, frequently excited dynamic imbalances may not have enough time to settle/spin-down to achieve relatively balanced forecasts before next DA, causing spurious error growth (Hu & Xue, 2007). Figure 13 shows the horizontal convergence fields at the first model level to highlight the dynamically unbalanced wind fields within the final analyses. Without using surface data, no significant convergence occurs west of the supercell (Figure 13a). However, with more cycles of surface data assimilated, the convergence increases rapidly west of the supercell (Figures 13b, 13c, and 13d), triggering spurious convection. This suggests more imbalance in the final analysis of allC_sfc compared to the other experiments. We attempted to reduce such wind field noise by increasing the decorrelation/influence radius of the dense surface DA, and the imbalance noise is much reduced when the influence radius is increased to 60 km. However, increasing the influence radius also smooths out detailed structures of the cold pools and gust fronts that are important for the development of near-surface vortices. Therefore, it is a dilemma associated with the inherent limitation of the 3DVAR technique, which uses static background error covariance, whose spatial decorrelation scales are empirically specified in ARPS 3DVar. Ensemble-derived flow-dependent covariances may help, but it is beyond the scope of this study.

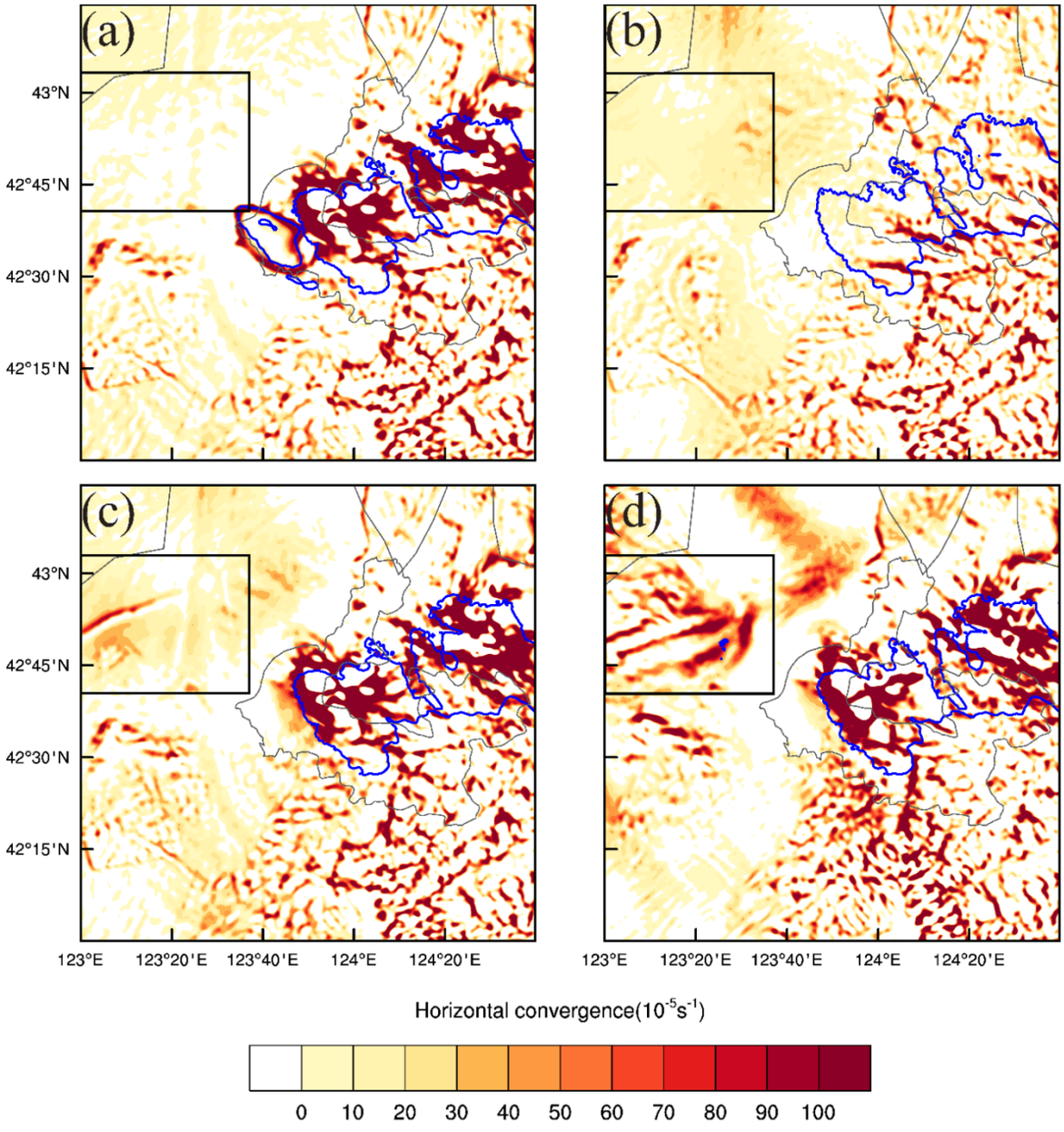

584

585 **Figure 13.** Horizontal convergence fields at the first model level (color shading, 1
586 × 10^{-5} s^{-1}), and 30-dBZ composite reflectivity (blue contours) of the final analyses
587 at 1730 LST for (a) no_sfc, (b) 1C_sfc, (c) last2C_sfc, and (d) allC_sfc. The black
588 boxes highlight the regions of significant dynamically imbalanced wind fields in
589 (d).

590

591 To explore the reason behind the differences in the intensity of simulated supercells during
592 the forecasts, we further investigate the final analysis fields from the four experiments. Figure
593 14 shows the mixed layer convective available potential energy (MLCAPE) from the final
594 analyses and the analysis increments of water vapor mixing ratio (q_v) at the lowest model level
595 above ground.

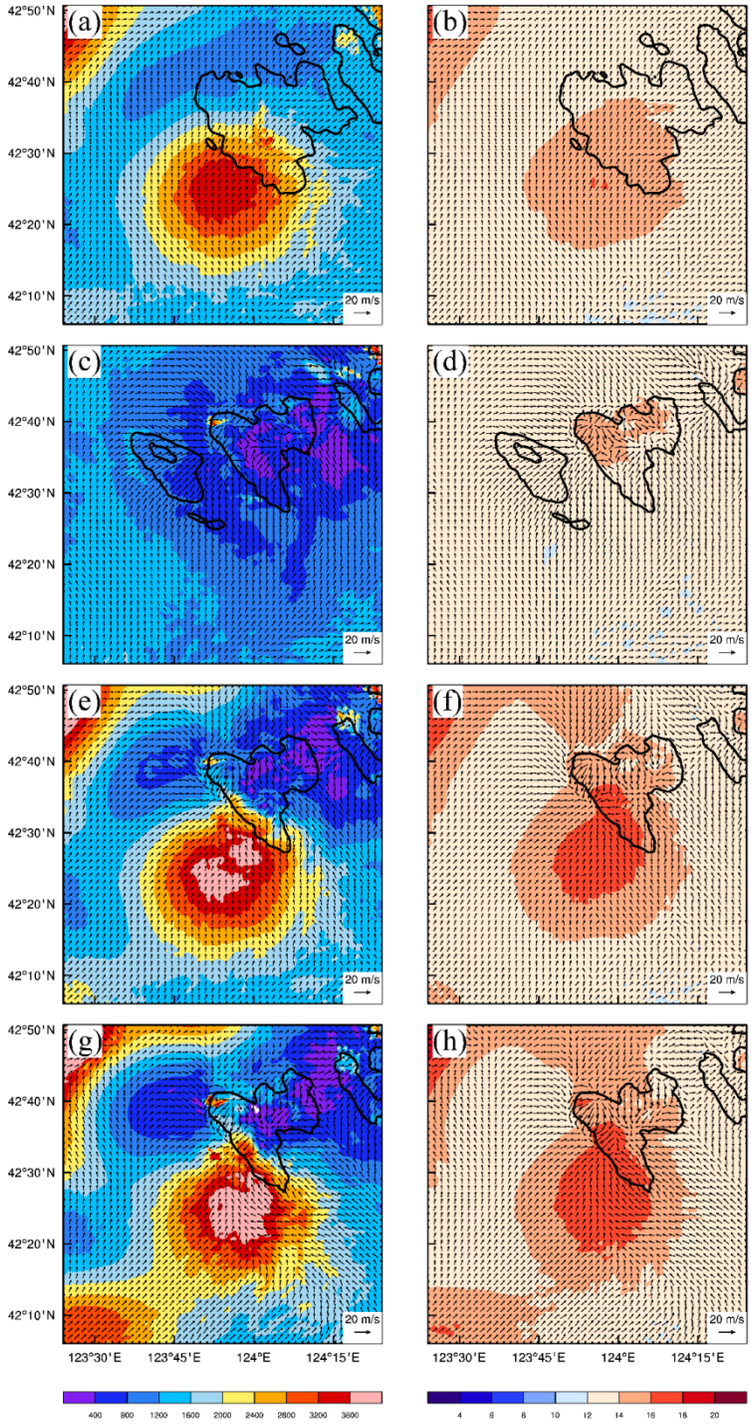

596

597 **Figure 14.** (left) Mixed layer convective available potential energy (MLCAPE,
598 shading, J kg^{-1}) and horizontal wind vectors (m s^{-1}), at the first model level above
599 ground of the final analyses at 1730 LST for (a) 1C_sfc, (c) no_sfc, (e) last2C_sfc,
600 and (g) allC_sfc. (right) As in left, but for analysis increment of water vapor mixing
601 ratio (q_v, shading, g kg^{-1}) before and after the DA cycles for (b) 1C_sfc, (d) no_sfc,
602 (f) last2C_sfc, and (h) allC_sfc. The heavy black contours in (c)-(h) denote the
603 boundary of 30-dBZ reflectivity at the first model level, but for 30-dBZ composite
604 reflectivity in (a)-(b).

605

606 Compared to no_sfc that does not assimilate any surface data (Figure 14c), the other three
607 experiments all exhibit a high-MLCAPE region southwest of the simulated supercell. The
608 presence of high MLCAPE in the inflow region allows the supercell to develop more vigorous
609 updrafts and produce stronger LMCs (Figures 11b, 11d, and 11e) and near-surface vortices
610 (Figures 12b, 12f, and 12g) during the forecast. A further investigation reveals that these
611 regions of high MLCAPE are mainly produced by near-surface q_v analysis increments of
612 similar patterns (Figures 14b, 14f, and 14h), as introduced by dense surface data during the DA
613 process. Apparently, as more (fewer) cycles of surface data are assimilated, more (less) q_v
614 increment is introduced, resulting in higher (lower) MLCAPE as in allC_sfc and last2C_sfc
615 (1C_sfc). It should be noted that the rounded patterns in these analysis fields can be attributed
616 to the super-observations made during the DA process and these data are analyzed with a
617 horizontal influence radii of 20 km.

618 The above analyses illustrated how the structures in the final analyses impact the evolution
619 of simulated supercell, LMC, and low-level vortices. The improvements in analyzed supercell
620 structures including the cold pool, and the better maintenance of near-surface vortices in the
621 forecasts highlight the key role of surface DA for the supercell predictions. Even though
622 significant forecast errors still remain, including timing error in the low-level vortex
623 development, the positive impacts of dense surface data, in addition to radar data, are evident.

624 Since last2C_sfc produces the best forecasts on the 450-m grid (Figure 7), a tornado-
625 resolving simulation with two additional grids nested inside its 450-m forecast is carried out,
626 and the results on the innermost 50-m grid will be presented in the next subsection.

627 **4.4 Tornado forecasts on the 50-m grid**

628 In this section, we examine the evolution and structures of the predicted tornado on the 50-
629 m grid nested inside the best-performing forecasts of last2C_sfc. Before diving into the
630 tornado-scale details, we first examine the storm-scale features of the simulated supercell and
631 its embedded LMC on the 50-m grid. Similar to the 450-m results, the predicted reflectivity
632 and radial velocity on the 50-m grid are remapped onto the 0.5° elevation of the SY radar. The
633 fields at 1842 LST are plotted in Figure 15.

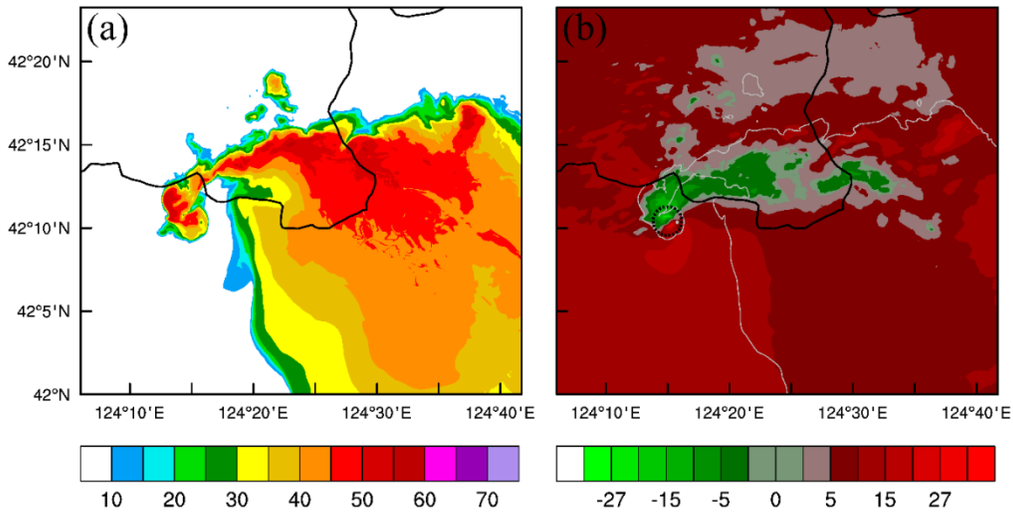

634

635 **Figure 15.** (a) Simulated reflectivity and (b) radial velocity from the 50-m
636 simulation at 1842 LST, projected to the 0.5° elevation of the SY radar. The white
637 contours in (b) outline the 30 dBZ reflectivity. The black dashed circle indicates
638 the tornado vortex region.

639

640 Compared to the 450-m forecast, the simulated reflectivity and radial velocity fields on the
641 50-m grid contain much more detailed structures. Specifically, it shows a more pronounced
642 hook echo containing an inward-spiraling reflectivity pattern at the northwestern tip of the
643 supercell (Figure 15a). For the radial velocity field, a finer-scale radial velocity couplet with
644 inbound-outbound velocity difference exceeding 70 m s^{-1} is located within the hook echo (see
645 the black circle in Figure 15b), indicating the presence of a stronger circulation than the one on
646 450-m grid and corresponding to a tornado or tornado-cyclone scale circulation.

647 To see the general evolution of the predicted tornado, time series of the maximum ζ,
648 maximum wind speed, and minimum perturbation pressure at the first model level above
649 ground, and the maximum w below 1-km height are plotted in Figure 16. A strong near-surface
650 vortex develops at around 1832 LST and reaches EF0 tornado intensity at around 1838 LST.
651 Here, a persistent near-surface vortex that lasts no shorter than 2 minutes with the surface wind
652 speed exceeding 30 m s^{-1} (the threshold of an EF0 tornado) is considered a tornado. The
653 predicted tornado quickly intensifies and reaches EF2 intensity with the maximum wind speed
654 exceeding 50 m s^{-1} at 1841 LST. The minimum pressure of about -13 hPa, maximum near-
655 surface ζ of more than 0.7 s^{-1}, and maximum w of over 40 m s^{-1} below 1 km near 1841 LST all
656 indicate that a well-defined tornado has formed at this time. After that, the tornado begins to
657 weaken and decreases to EF0 intensity at 1843 LST. The maximum ζ is restored above 0.5 s^{-1}

around 1849 LST. By 1850 LST, the tornado vortex is mostly dissipated. The tornado with EF0 intensity or above therefore lasts for about 5 minutes in the simulation.

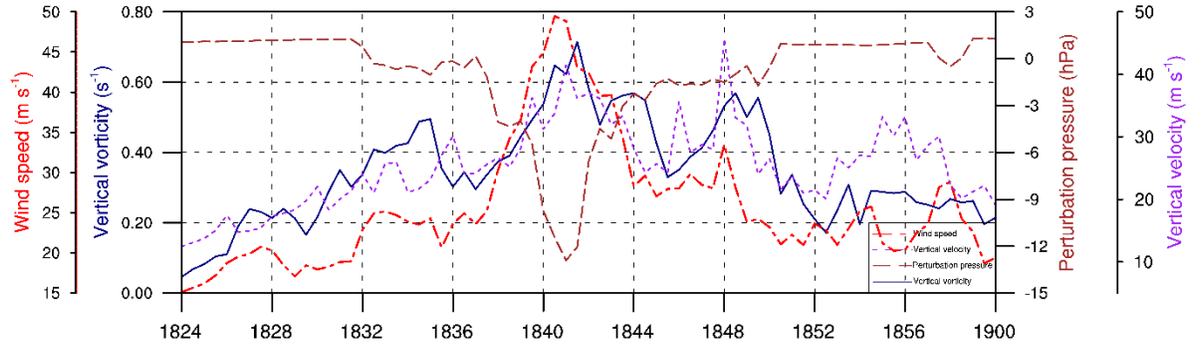

Figure 16. Time series of predicted maximum ζ (dark blue, s^{-1}), wind speed (red, m s^{-1}), and minimum perturbation pressure (brown, hPa) at the first model level above ground, and the maximum w below 1-km height (purple, m s^{-1}) on the 50-m grid from 1824 to 1900 LST. Data are plotted in a 30-second interval.

A composite of ζ at the lowest model level on the 50-m grid at a number of times is shown in Figure 17 to visualize the evolution of the simulated tornado vortex. A small vortex first forms at 1830 LST. It then increases in size and intensity and establishes a well-defined strong vortex with a 'one-cell' structure (Davies-Jones et al., 2001), with the maximum vorticity located at the vortex center from 1832:30 to 1835:30 LST. Shortly after, it quickly evolves into a 'two-cell' structure (Davies-Jones et al., 2001) with a high-vorticity ring forming around the vortex center at 18:36:30 LST. This vorticity ring becomes stronger and more axisymmetric from 1838:30 and remains so through 1842:30. By 1843:30, the vortex ring expands in diameter and appears to become unstable. The vortex ring becomes discontinuous, and strong axis-asymmetry starts to develop. Such evolution is usually accompanied by the development of a downdraft at the center of the vortex that reaches the ground creating divergence. Sub-vortices appear to develop on the vortex ring by 1844:30, due to barotropic instability triggering vortex Rossby waves (Huang & Xue, 2023). The closed ring structure is maintained for about 7 minutes from 18:36:30 to 18:43:30 LST then breaks into a ring of multiple sub-vortices at 18:44:30 LST. With the instability and strong divergence at the center of the vortex, the tornado vortex quickly breaks down and dissipates in the ensuing couple of minutes (Figure 17). Similar evolution was found in the simulation of a supercell tornado that occurred in Funing, Jiangsu, China in 2016 (see Figure 12 of Sun et al. (2019)), except the simulated sub-vortices in their case lasted much longer. Xue et al. (2014) also obtained similar general evolution of a supercell

685 tornado that occurred in Oklahoma, USA (see their Fig. 14), and such a sequence of evolution
686 appear common to several existing real-case simulations of tornado life cycle.

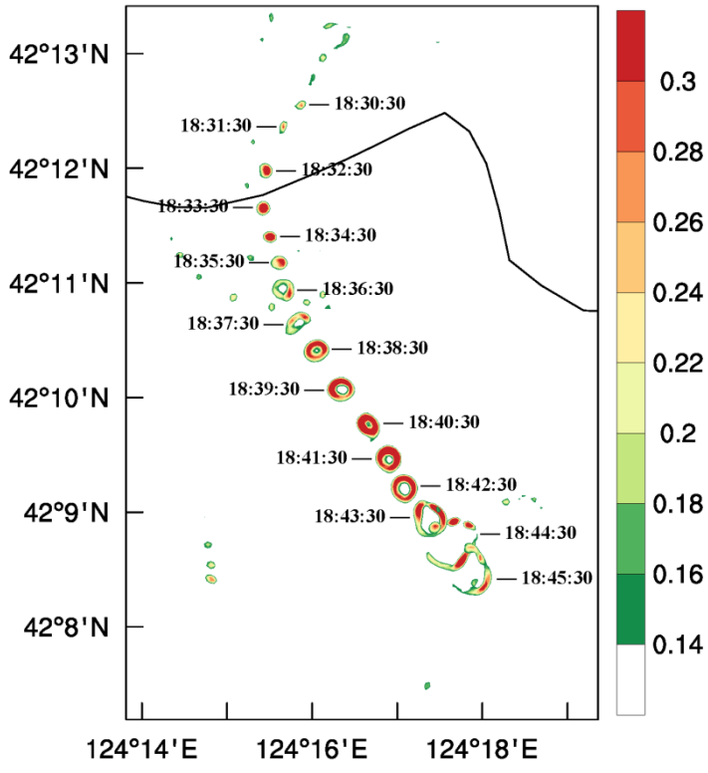

687

688 **Figure 17.** Overview of large positive ζ (color shaded, s^{-1}) at the lowest model level
689 above ground for the simulated tornado plotted each minute between 18:28:30 to
690 18:45:30 LST 3 July 2019.

691

692 The structures of the simulated tornado are further illustrated by the horizontal and vertical
693 cross sections in Figure 18, showing the *w* and *ζ* fields through the tornado at 1835, 1842, and
694 1844:30 LST. They correspond to the times when the tornado forms at the one-cell stage, the
695 tornado reaches peak intensity in the two-cell stage, and the tornado vortex breaks down into
696 sub-vortices at the multiple-vortex stage, respectively.

697 At 1835 LST, the tornado has a well-defined one-cell structure with the vortex center
698 surrounded by cyclonically rotating winds at the tip of the hook echo (Figure 18a). A
699 southwest-northeast-oriented vertical cross section through the vortex center shows that the ζ
700 maximum is near the surface and the vorticity decreases with height, which is characteristic of
701 a fully developed tornado (Huang & Xue, 2025b). Meanwhile, upward motion is generally
702 associated with the ζ column although the strongest updrafts are not located at the vortex center
703 but at the edge of the large vorticity column with *w* at the vorticity column center being < 2 m
704 s^{-1} while *w* >10 m s^{-1} at ~ 800 m height on the south side (Figure 18b). Huang and Xue (2025a)

explain such a structure as the result of negative downward dynamic pressure gradient force (DPGF) due to strong near-ground rotation within the vortex, and positive upward DPGF off the center of the vortex due to strong flow convergence and deformation associated with the splat term in the diagnostic pressure equation. Weak downdrafts are found outside of the vortex center close to the ground (Figure 18b), which should be at least partially due to the compensating circulation outside the strong updrafts.

By 1842 LST, the predicted tornado has entered into the two-cell stage with the largest ζ being concentrated in a ring and displaced from the vortex center (Figure 18c and Figure 17). The cyclonically rotating winds around the vortex center are increased significantly and exceed the EF2 intensity at this time. In the west-east-oriented vertical cross section through the vortex ring (along line C-D in Figure 18c), the maximum ζ remains near the ground and is located at the vorticity ring. The maximum w is located immediately outside of the vortex ring, where radial flow convergence is the strongest. On the west side of the vortex, the updraft is stronger and more upright, and its low-level maximum is found at about 1-km height. The maximum on the east side of the vortex is closer to the ground (Figure 18d). Meanwhile, a strong downdraft with $|w| > 8$ m s^{-1} reaching the ground surface has developed at the vortex center, due to the downward PGF associated with strong near-surface rotation discussed above, which has also been referred to as the vortex-valve effect (Trapp, 2000). This downdraft extends from the surface to about 2 km with its maximum value at about 1-km height (Figure 18d). As suggested earlier, further intensification of this vortex-core downdraft can cause the demise of the tornado.

At 1844:30 LST, multiple sub-vortices are seen to have developed along the vorticity ring and are revolving around the tornado vortex center (Figure 18e). The horizontal wind speed decreases a little due to the overall weakening of the tornado vortex (Figure 16). In the vertical cross section through the two strongest sub-vortices, the sub-vortices are relatively shallow and vertically tilted (Figure 18f). The updraft cores are collocated with the sub-vortices; it extends to ~2 km on the north side but is shallower on the south side; this is consistent with the results presented in Huang and Xue (2025a) that the low-level flows converging into the tornado vortex from the north side are stronger while occlusion downdrafts are generally found on the southeast side outside the vorticity ring. At 1844:30 LST, the downdraft at the vortex center has been enhanced significantly and extends to above 2-km height (Figure 18f), which causes stronger divergent flow near the ground within the vortex (Figure 18e). This divergent flow inhibits the further development of the tornado vortex and leads to the quick dissipation of the tornado (Figures 16 and 17).

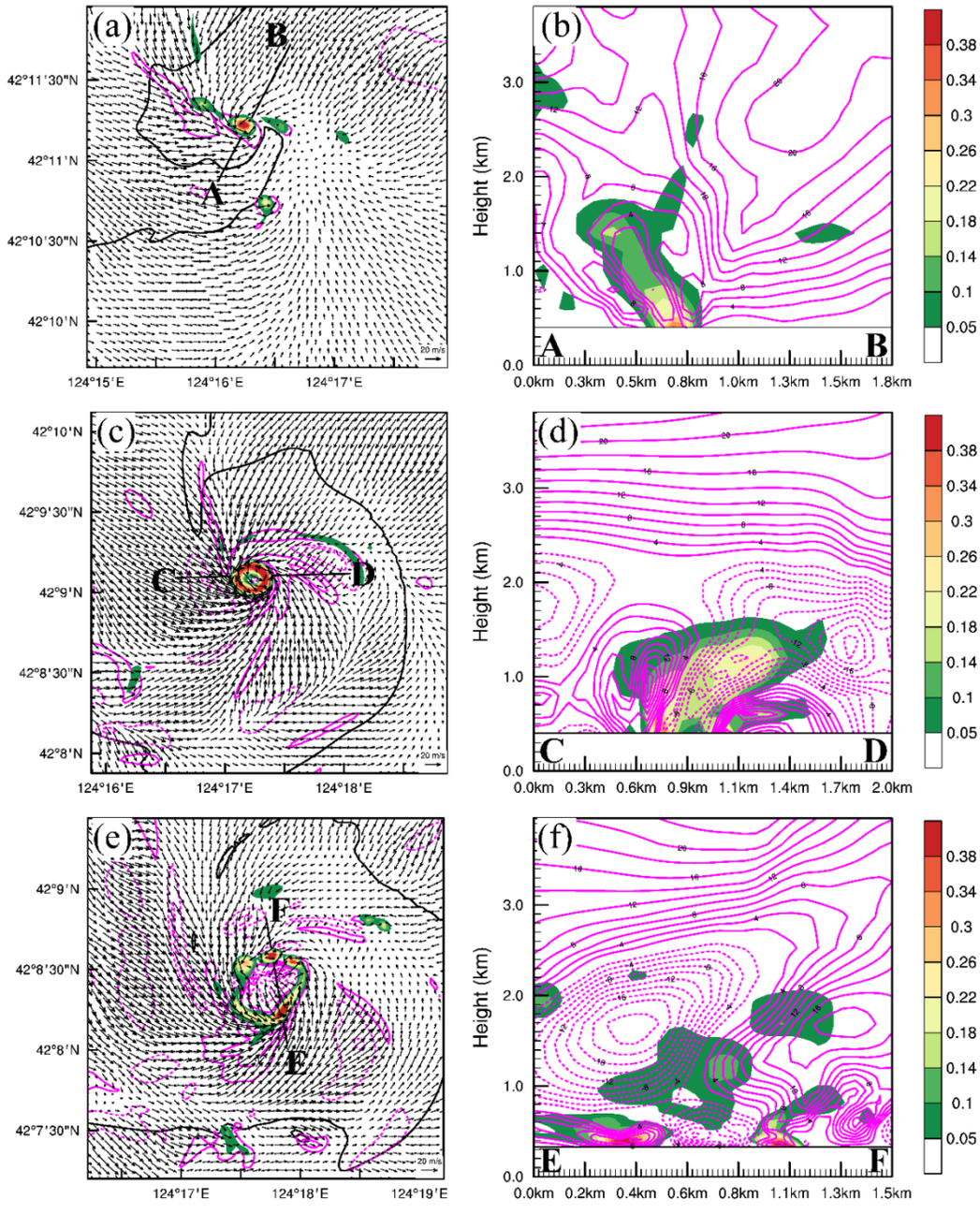

738

739 **Figure 18.** (a, c, e) Horizontal cross sections of predicted ζ (color shaded, s^{-1}),
740 horizontal wind vectors, 30-dBZ reflectivity (thick black contours), and w (magenta
741 contours every 1 m s^{-1} with negative contours dashed) at the first model level above
742 ground and (b, d, f) vertical cross sections of ζ (color shaded, s^{-1}) and w (magenta
743 contours every 2 m s^{-1} with negative contours dashed) at (a, b) 1835:00, (c, d)
744 1842:00, and (e, f) 1844:30 LST. The locations of the vertical cross-sections are
745 marked by straight lines in (a, c, e) with the orientation of cross-sections labeled
746 with A-B, C-D, E-F, respectively.

747 Although the predicted tornado strength is weaker than observed and there are timing and
748 location errors between the forecast and observations, the general track length, orientation, as
749 well as the life cycle of the predicted tornado agree reasonably well with the observations. The

overall southeastward displacement of the tornado track appears to be more due to the southeastward displacement of the predicted supercell (see Figure 10) than due to the relative position of the tornado within the storm. Since the starting time of the free forecast is slightly later than the real-world tornadogenesis time due to the need to assimilate sufficient radar observations and to give the model needed spin-up time, the timing and location errors are difficult to avoid completely. Similar degrees of errors are often found in limited available real tornado simulation/prediction studies, even when multi-volumes of radar data are assimilated (e.g., Xue et al., 2014). Large differences are also found in the tracks and longevity of simulated tornadoes among the ensemble members initialized with EnKF analyses in Snook et al. (2019). The most encouraging part of our results is the general success in obtaining tornadoes or tornado-like vortices with realistic structures and evolutions that have reasonable correspondence with the observed supercell tornado. The results also show that a state-of-the-science NWP model run at a LES resolution, with assimilation of high-resolution convective-scale data, has the intrinsic ability to produce realistic forecast of tornadoes. This study demonstrates this for the first time for a tornado case in China, assimilating data from multiple operational radars of diverse types and dense surface station data. Given the large uncertainties and low predictability of tornadoes (Markowski, 2020), ensemble probabilistic forecasting is needed for the most effective forecast guidance (Stensrud et al., 2009).

5. Summary and discussion

In this study, the 3 July 2019 Kaiyuan, China tornadic supercell and its embedded tornado are simulated using the WRF model, initialized from a set of initial conditions that assimilated Doppler weather radar and high-resolution surface observations using the ARPS 3DVar and cloud analysis system. The WRF model is configured with five levels of nested grids with the DA performed on the third-level 450-m grid. The innermost grid of 50-m grid spacing serves to explicitly simulate the Kaiyuan tornado.

Four experiments with reflectivity and radial velocity data from multiple radars assimilated in every cycle at 5-minute intervals over a 30-minute period, or in the last cycle at the end are conducted, while additional observations from dense surface stations are assimilated within the last cycle only (experiment 1C_sfc), in the last two cycles (last2C_sfc), in all cycles (allC_sfc) or in no cycle at all (no_sfc). Emphasis is placed on the impact of the additional surface data on the supercell analysis and prediction, and the subsequent simulation/prediction of the embedded tornado. The root-mean squared innovations (RMSIs) of the analyses calculated

against observed reflectivity and radial velocity are effectively reduced in all experiments after each cycle when radar data are assimilated. With additional surface data assimilation, the RMSIs of forecast reflectivity and radial velocity from 1C_sfc, last2C_sfc, and allC_sfc are lower than those of no_sfc that assimilates no surface data. The RMSIs of the analyses calculated against surface observations, including station pressure, temperature, dewpoint, wind speed, and *u, v* components of surface wind, are also reduced significantly after each cycle of surface DA. Without surface DA, the RMSIs in no_sfc are the highest at the final analysis time and remain the highest throughout the subsequent forecast.

The morphology and structures of the analyzed supercells in all experiments are improved by radar DA. The experiments assimilating surface data in multiple cycles produce better near-surface features, especially in terms of better-constructed cold pools. Forecasting results also demonstrate clear improvements when dense surface data are assimilated. Specifically, a well-defined hook echo and strong low-level mesocyclone circulation are produced with surface DA, while the hook echo and mesocyclone are less organized or weaker in no_sfc. In addition, the supercell updraft and near-surface rotation in the forecasts are stronger when surface data are assimilated.

No strong near-surface vortex is produced when surface data are not assimilated due to the poor representation of the simulated cold pool. Although rapidly cycled surface DA can improve the cold pool representation during the forecasts, it also causes significant spurious convection due to imbalances introduced, which also negatively impacts the maintenance of the near-surface vortex. Further investigation of the final analyses provide insights on the different intensities of the simulated supercells during the forecasts. When more cycles of surface data are assimilated, higher MLCAPE is found in the final analyses, resulting in a more intense supercell.

Based on the best-performing 450-m forecast of the tornadic supercell, two more grids with 150 m and 50 m grid spacings are nested within it to explicitly predict the Kaiyuan tornado. The simulated supercell on the 50-m grid exhibits more detailed storm-scale structures and tornado-scale circulations than on the 450-m grid. At the tornado-resolving 50-m resolution, the model predicts realistically the genesis and evolution of a tornado, which evolves through one-cell, two-cell, and multiple sub-vortices stages. Horizontal and vertical cross-sections through the simulated tornado vortex at the three stages show fine-scale structures that are consistent with the findings in previous theoretical, numerical, and observational studies of tornadoes (Rotunno & Klemp, 1985; Lewellen et al., 1997; Davies-Jones et al., 2001; Wurman, 2002; Lee & Wurman, 2005; Xue et al., 2014; Mashiko & Niino, 2017; Sun et al., 2019).

Although there are timing and location errors between the predicted and observed tornadoes, the track and life cycle of the predicted tornado agree reasonably well with observations. The similarity between the storm-relative locations of the predicted and observed tornado provides additional evidence that the dynamical processes involved in the two counterparts are in general consistent.

In all, the high-resolution DA and simulation/prediction experiments conducted in this study demonstrate the importance of assimilating high-resolution surface observations, in addition to those of radars, to improve the prediction of the tornadic supercell and its embedded tornado. The two types of observations are complementary and cover mainly in-storm conditions and the storm environment, respectively. To the best of the authors' knowledge, this study represents the first real-case study in which a tornado in China is explicitly predicted through the assimilation of radar and dense surface observations. The presented results are encouraging in the pursuit of a warn-on-forecast concept (Stensrud et al., 2009) aiming at numerically predicting tornadoes to achieve longer tornado warning lead times and higher spatial accuracy from an operational forecasting point of view. In the meantime, some special treatment had to be made in the experiments to obtain the desirable forecasting results, which are partly due to limitations of observations in spatial and temporal scales and the assimilation method used. Therefore, studies of additional tornado cases and using more advanced DA methods are warranted to better understand the predictability aspects of the tornado prediction science. The model simulation data sets can also be analyzed in detail to understand dynamical processes for tornadoes, as has been done for the Funing tornado case (e.g., Huang & Xue, 2023, 2025a).

Funding Statement.

This work was primarily supported by NSFC Grant 41730965.

Acknowledgments.

The first author acknowledges the hosting by CAPS, University of Oklahoma of his visit, where most of this research was conducted. Computing was mostly done on supercomputer Expanse at the San Diago Supercomputing Center, with resources allocated through the ACCESS program.

Data Availability Statement.

ARPS model can be downloaded online (available at http://arps.caps.ou.edu/). CAPS Polarimetric Radar data Simulator (CAPS-PRS) can be downloaded online (available at https://arps.caps.ou.edu/downloadpyDualPol.html). ERA5 reanalysis data can be downloaded online (available at https://doi.org/10.24381/cds.bd0915c6). Radar data and dense automatic weather station (AWS) data are provided by the Liaoning Meteorological Bureau, Jilin Meteorological Service, and Heilongjiang Meteorological Bureau. The processed data sets within this paper, including the radar and AWS datasets, radar emulation, data assimilation and numerical simulation outputs can be found at Harvard Dataverse (https://doi.org/10.7910/DVN/A6RSTY).

REFERENCES

Brock, F. V., Crawford, K. C., Elliott, R. L., Cuperus, G. W., Stadler, S. J., Johnson, H. L., & Eilts, M. D. (1995). The Oklahoma Mesonet: A Technical Overview. *Journal of Atmospheric and Oceanic Technology*, 12, 5-19. https://doi.org/10.1175/1520-0426(1995)012<0005:TOMATO>2.0.CO;2

Chen, H., Chen, Y., Gao, J., Sun, T., & Carlin, J. T. (2020). A radar reflectivity data assimilation method based on background-dependent hydrometeor retrieval: An observing system simulation experiment. *Atmospheric Research*, 243, 105022. https://doi.org/10.1016/j.atmosres.2020.105022

Chen, X., Zhao, K., Sun, J., Zhou, B., & Lee, W.-C. (2016). Assimilating surface observations in a four-dimensional variational Doppler radar data assimilation system to improve the analysis and forecast of a squall line case. *Advances in Atmospheric Sciences*, 33, 1106-1119. https://doi.org/10.1007/s00376-016-5290-0

Collins, W., Rasch, P. J., Boville, B. A., McCaa, J., Williamson, D. L., Kiehl, J. T., et al. (2004). Description of the NCAR Community Atmosphere Model (CAM 3.0). Boulder, CO: National Center for Atmospheric Research

Davies-Jones, R., Trapp, R. J., & Bluestein, H. B. (2001). Tornadoes and Tornadic Storms. *Meteorological Monographs*, 28, 167-222. https://doi.org/10.1175/0065-9401-28.50.167

Dawson, D. T., Wicker, L. J., Mansell, E. R., & Tanamachi, R. L. (2012). Impact of the Environmental Low-Level Wind Profile on Ensemble Forecasts of the 4 May 2007 Greensburg, Kansas, Tornadic Storm and Associated Mesocyclones. *Monthly Weather Review*, 140, 696-716. https://doi.org/10.1175/mwr-d-11-00008.1

Dawson, D. T., Xue, M., Milbrandt, J. A., & Shapiro, A. (2015). Sensitivity of Real-Data Simulations of the 3 May 1999 Oklahoma City Tornadic Supercell and Associated Tornadoes to Multimoment Microphysics. Part I: Storm- and Tornado-Scale Numerical Forecasts. *Monthly Weather Review*, 143, 2241-2265. https://doi.org/10.1175/mwr-d-14-00279.1

Dong, J., Xue, M., & Droegemeier, K. (2011). The analysis and impact of simulated high-resolution surface observations in addition to radar data for convective storms with an

ensemble Kalman filter. *Meteorology and Atmospheric Physics*, 112, 41-61. https://doi.org/10.1007/s00703-011-0130-3

Fan, Z., Zhu, K., & Xue, M. (2023). Decay processes and statistical characteristics of Continental Northeast China cold vortex from April to September. *Acta Meteorologica Sinica*. https://doi.org/10.11676/qxxb2023.20220171

Federico, S., Torcasio, R. C., Avolio, E., Caumont, O., Montopoli, M., Baldini, L., et al. (2019). The impact of lightning and radar reflectivity factor data assimilation on the very short-term rainfall forecasts of RAMS@ISAC: application to two case studies in Italy. *Natural Hazards and Earth System Sciences*, 19, 1839-1864. https://doi.org/10.5194/nhess-19-1839-2019

Fiebrich, C. A. (2009). History of surface weather observations in the United States. *Earth-Science Reviews*, 93, 77-84. https://doi.org/10.1016/j.earscirev.2009.01.001

Gao, J., Smith, T. M., Stensrud, D. J., Fu, C., Calhoun, K., Manross, K. L., et al. (2013). A Real-Time Weather-Adaptive 3DVAR Analysis System for Severe Weather Detections and Warnings. *Weather and Forecasting*, 28, 727-745. https://doi.org/10.1175/WAF-D-12-00093.1

Gao, J., & Stensrud, D. J. (2012). Assimilation of Reflectivity Data in a Convective-Scale, Cycled 3DVAR Framework with Hydrometeor Classification. *Journal of the Atmospheric Sciences*, 69, 1054-1065. https://doi.org/10.1175/JAS-D-11-0162.1

Gao, J., Xue, M., Brewster, K., & Droegemeier, K. K. (2004). A Three-Dimensional Variational Data Analysis Method with Recursive Filter for Doppler Radars. *Journal of Atmospheric and Oceanic Technology*, 21, 457-469. https://doi.org/10.1175/1520-0426(2004)021<0457:ATVDAM>2.0.CO;2

Gao, J., Xue, M., Shapiro, A., & Droegemeier, K. K. (1999). A Variational Method for the Analysis of Three-Dimensional Wind Fields from Two Doppler Radars. *Monthly Weather Review*, 127, 2128-2142. https://doi.org/10.1175/1520-0493(1999)127<2128:AVMFTA>2.0.CO;2

Hersbach, H., Bell, B., Berrisford, P., Hirahara, S., Horányi, A., Muñoz-Sabater, J., et al. (2020). The ERA5 global reanalysis. *Quarterly Journal of the Royal Meteorological Society*, 146, 1999-2049. https://doi.org/10.1002/qj.3803

Hu, M., & Xue, M. (2007). Impact of Configurations of Rapid Intermittent Assimilation of WSR-88D Radar Data for the 8 May 2003 Oklahoma City Tornadic Thunderstorm Case. *Monthly Weather Review*, 135, 507-525. https://doi.org/10.1175/mwr3313.1

Hu, M., Xue, M., & Brewster, K. (2006a). 3DVAR and Cloud Analysis with WSR-88D Level-II Data for the Prediction of the Fort Worth, Texas, Tornadic Thunderstorms. Part I: Cloud Analysis and Its Impact. *Monthly Weather Review*, 134, 675-698. https://doi.org/10.1175/mwr3092.1

Hu, M., Xue, M., Gao, J., & Brewster, K. (2006b). 3DVAR and Cloud Analysis with WSR-88D Level-II Data for the Prediction of the Fort Worth, Texas, Tornadic Thunderstorms. Part II: Impact of Radial Velocity Analysis via 3DVAR. *Monthly Weather Review*, 134, 699-721. https://doi.org/10.1175/MWR3093.1

Huang, W., & Xue, M. (2023). Subvortices within a Numerically Simulated Tornado: The Role of Unstable Vortex Rossby Waves. *Journal of the Atmospheric Sciences*, 80, 2503-2529. https://doi.org/10.1175/JAS-D-22-0237.1

——. (2025a). How are Vorticity Rivers in Supercell Storms Produced and Are They Important Vorticity Sources for Tornadoes? *Journal of the Atmospheric Sciences*. https://doi.org/10.1175/JAS-D-24-0227.1

——. (2025b). What Forces the Rapid Vertical Acceleration and Vorticity Intensification Near Ground in Tornadoes? Diagnostic Analysis based on a Numerically Simulated Real Tornado. *Journal of the Atmospheric Sciences*. https://doi.org/10.1175/JAS-D-25-0033.1

Jung, Y., Xue, M., & Tong, M. (2012). Ensemble Kalman Filter Analyses of the 29–30 May 2004 Oklahoma Tornadic Thunderstorm Using One- and Two-Moment Bulk Microphysics Schemes, with Verification against Polarimetric Radar Data. *Monthly Weather Review*, 140, 1457-1475. https://doi.org/10.1175/mwr-d-11-00032.1

Jung, Y., Xue, M., & Zhang, G. (2010). Simulations of Polarimetric Radar Signatures of a Supercell Storm Using a Two-Moment Bulk Microphysics Scheme. *Journal of Applied Meteorology and Climatology*, 49, 146-163. https://doi.org/10.1175/2009JAMC2178.1

Jung, Y., Zhang, G., & Xue, M. (2008). Assimilation of Simulated Polarimetric Radar Data for a Convective Storm Using the Ensemble Kalman Filter. Part I: Observation Operators for Reflectivity and Polarimetric Variables. *Monthly Weather Review*, 136, 2228-2245. https://doi.org/10.1175/2007MWR2083.1

Landolt, S. D., Lave, J. S., Jacobson, D., Gaydos, A., DiVito, S., & Porter, D. (2019). The Impacts of Automation on Present Weather–Type Observing Capabilities across the Conterminous United States. *Journal of Applied Meteorology and Climatology*, 58, 2699-2715. https://doi.org/10.1175/JAMC-D-19-0170.1

Lee, W.-C., & Wurman, J. (2005). Diagnosed Three-Dimensional Axisymmetric Structure of the Mulhall Tornado on 3 May 1999. *Journal of the Atmospheric Sciences*, 62, 2373-2393. https://doi.org/10.1175/JAS3489.1

Lewellen, W. S., Lewellen, D. C., & Sykes, R. I. (1997). Large-Eddy Simulation of a Tornado's Interaction with the Surface. *Journal of the Atmospheric Sciences*, 54, 581-605. https://doi.org/10.1175/1520-0469(1997)054<0581:LESOAT>2.0.CO;2

Li, H., Xue, M., Zhu, K., & Xu, X. (2024). Initiation of a Supercell by Convectively Generated Gravity Waves in the Simulated Kaiyuan Tornadic Event of 3 July 2019. *Monthly Weather Review*, 152, 2587-2608. https://doi.org/10.1175/MWR-D-23-0248.1

Li, R., Sun, J., Zhang, Q., & Jensen, A. A. (2022). Model Predictability of Hail Precipitation with a Moderate Hailstorm Case. Part I: Impact of Improved Initial Conditions by Assimilating High-Density Observations. *Monthly Weather Review*, 150, 2675-2696. https://doi.org/10.1175/MWR-D-21-0329.1

Liu, H., & Xue, M. (2008). Prediction of Convective Initiation and Storm Evolution on 12 June 2002 during IHOP_2002. Part I: Control Simulation and Sensitivity Experiments. *Monthly Weather Review*, 136, 2261-2282. https://doi.org/10.1175/2007MWR2161.1

Luo, L., Xue, M., & Zhu, K. (2020). The Initiation and Organization of a Severe Hail-Producing Mesoscale Convective System in East China: A Numerical Study. *Journal of Geophysical Research: Atmospheres*, 125, e2020JD032606. https://doi.org/10.1029/2020JD032606

Markowski, P. M. (2020). What is the Intrinsic Predictability of Tornadic Supercell Thunderstorms? *Monthly Weather Review*, 148, 3157-3180. https://doi.org/10.1175/MWR-D-20-0076.1

975 Markowski, P. M., & Richardson, Y. P. (2014). The Influence of Environmental Low-Level
976 Shear and Cold Pools on Tornadogenesis: Insights from Idealized Simulations. *Journal of the*
977 *Atmospheric Sciences*, 71, 243-275. https://doi.org/10.1175/JAS-D-13-0159.1

978 Marquis, J., Richardson, Y., Markowski, P., Dowell, D., & Wurman, J. (2012). Tornado
979 Maintenance Investigated with High-Resolution Dual-Doppler and EnKF Analysis. *Monthly*
980 *Weather Review*, 140, 3-27. https://doi.org/10.1175/MWR-D-11-00025.1

981 Mashiko, W. (2016). A Numerical Study of the 6 May 2012 Tsukuba City Supercell Tornado.
982 Part I: Vorticity Sources of Low-Level and Midlevel Mesocyclones. *Monthly Weather*
983 *Review*, 144, 1069-1092. https://doi.org/10.1175/MWR-D-15-0123.1

984 Mashiko, W., & Niino, H. (2017). Super High-Resolution Simulation of the 6 May 2012
985 Tsukuba Supercell Tornado: Near-Surface Structure and Its Evolution. *SOLA*, 13, 135-139.
986 https://doi.org/10.2151/sola.2017-025

987 Mashiko, W., Niino, H., & Kato, T. (2009). Numerical Simulation of Tornadogenesis in an
988 Outer-Rainband Minisupercell of Typhoon Shanshan on 17 September 2006. *Monthly*
989 *Weather Review*, 137, 4238-4260. https://doi.org/10.1175/2009MWR2959.1

990 Meng, Z., Bai, L., Zhang, M., Wu, Z., Li, Z., Pu, M., et al. (2018). The Deadliest Tornado
991 (EF4) in the Past 40 Years in China. *Weather and Forecasting*, 33, 693-713.
992 https://doi.org/10.1175/waf-d-17-0085.1

993 Meng, Z., Yao, D., Bai, L., Zheng, Y., Xue, M., Zhang, X., et al. (2016). Wind estimation
994 around the shipwreck of Oriental Star based on field damage surveys and radar observations.
995 *Science Bulletin*, 61, 330-337. https://doi.org/10.1007/s11434-016-1005-2

996 Morrison, H., & Grabowski, W. W. (2008). A Novel Approach for Representing Ice
997 Microphysics in Models: Description and Tests Using a Kinematic Framework. *Journal of*
998 *the Atmospheric Sciences*, 65, 1528-1548. https://doi.org/10.1175/2007jas2491.1

999 Pleim, J. E. (2006). A Simple, Efficient Solution of Flux–Profile Relationships in the
1000 Atmospheric Surface Layer. *Journal of Applied Meteorology and Climatology*, 45, 341-347.
1001 https://doi.org/10.1175/jam2339.1

1002 ——. (2007). A Combined Local and Nonlocal Closure Model for the Atmospheric
1003 Boundary Layer. Part I: Model Description and Testing. *Journal of Applied Meteorology and*
1004 *Climatology*, 46, 1383-1395. https://doi.org/10.1175/jam2539.1

1005 Putnam, B., Xue, M., Jung, Y., Snook, N., & Zhang, G. (2019). Ensemble Kalman Filter
1006 Assimilation of Polarimetric Radar Observations for the 20 May 2013 Oklahoma Tornadic
1007 Supercell Case. *Monthly Weather Review*, 147, 2511-2533. https://doi.org/10.1175/MWR-D-
1008 18-0251.1

1009 Putnam, B. J., Xue, M., Jung, Y., Snook, N., & Zhang, G. (2014). The Analysis and
1010 Prediction of Microphysical States and Polarimetric Radar Variables in a Mesoscale
1011 Convective System Using Double-Moment Microphysics, Multinetwork Radar Data, and the
1012 Ensemble Kalman Filter. *Monthly Weather Review*, 142, 141-162.
1013 https://doi.org/10.1175/MWR-D-13-00042.1

1014 Rotunno, R., & Klemp, J. (1985). On the Rotation and Propagation of Simulated Supercell
1015 Thunderstorms. *Journal of Atmospheric Sciences*, 42, 271-292. https://doi.org/10.1175/1520-
1016 0469(1985)042<0271:Otrapo>2.0.Co;2

1017 Schenkman, A. D., Xue, M., & Shapiro, A. (2012). Tornadogenesis in a Simulated
1018 Mesovortex within a Mesoscale Convective System. *Journal of the Atmospheric Sciences*, 69,
1019 3372-3390. https://doi.org/10.1175/JAS-D-12-038.1

1020 Schenkman, A. D., Xue, M., Shapiro, A., Brewster, K., & Gao, J. (2011). Impact of CASA
1021 Radar and Oklahoma Mesonet Data Assimilation on the Analysis and Prediction of Tornadic
1022 Mesovortices in an MCS. *Monthly Weather Review*, 139, 3422-3445.
1023 https://doi.org/10.1175/MWR-D-10-05051.1

1024 Skamarock, W. C., Klemp, J. B., Dudhia, J., Gill, D. O., Barker, D. M., Duda, M. G., et al.
1025 (2008). A Description of the Advanced Research WRF Version 3. Boulder, CO: National
1026 Center for Atmospheric Research

1027 Snook, N., & Xue, M. (2008). Effects of microphysical drop size distribution on
1028 tornadogenesis in supercell thunderstorms. *Geophysical Research Letters*, 35.
1029 https://doi.org/10.1029/2008GL035866

1030 Snook, N., Xue, M., & Jung, Y. (2015). Multiscale EnKF Assimilation of Radar and
1031 Conventional Observations and Ensemble Forecasting for a Tornadic Mesoscale Convective
1032 System. *Monthly Weather Review*, 143, 1035-1057. https://doi.org/10.1175/MWR-D-13-
1033 00262.1

1034 ——. (2019). Tornado-Resolving Ensemble and Probabilistic Predictions of the 20 May 2013
1035 Newcastle–Moore EF5 Tornado. *Monthly Weather Review*, 147, 1215-1235.
1036 https://doi.org/10.1175/MWR-D-18-0236.1

1037 Stensrud, D. J., & Gao, J. (2010). Importance of Horizontally Inhomogeneous Environmental
1038 Initial Conditions to Ensemble Storm-Scale Radar Data Assimilation and Very Short-Range
1039 Forecasts. *Monthly Weather Review*, 138, 1250-1272.
1040 https://doi.org/10.1175/2009MWR3027.1

1041 Stensrud, D. J., Wicker, L. J., Xue, M., Dawson, D. T., Yussouf, N., Wheatley, D. M., et al.
1042 (2013). Progress and challenges with Warn-on-Forecast. *Atmospheric Research*, 123, 2-16.
1043 https://doi.org/10.1016/j.atmosres.2012.04.004

1044 Stensrud, D. J., Xue, M., Wicker, L. J., Kelleher, K. E., Foster, M. P., Schaefer, J. T., et al.
1045 (2009). Convective-Scale Warn-on-Forecast System: A Vision for 2020. *Bulletin of the*
1046 *American Meteorological Society*, 90, 1487-1500. https://doi.org/10.1175/2009BAMS2795.1

1047 Sun, J., Xue, M., Wilson, J. W., Zawadzki, I., Ballard, S. P., Onvlee-Hooimeyer, J., et al.
1048 (2014). Use of NWP for Nowcasting Convective Precipitation: Recent Progress and
1049 Challenges. *Bulletin of the American Meteorological Society*, 95, 409-426.
1050 https://doi.org/10.1175/BAMS-D-11-00263.1

1051 Sun, L., Zheng, X., & Wang, Q. (1994). The climatological characteristics of northeast cold
1052 vortex in China. *Quart J Appl Meteor*, 5, 297-303

1053 Sun, Z., Xue, M., Zhu, K., & Zhou, B. (2019). Prediction of an EF4 supercell tornado in
1054 Funing, China: Resolution dependency of simulated tornadoes and their structures.
1055 *Atmospheric Research*, 229, 175-189. https://doi.org/10.1016/j.atmosres.2019.06.019

1056 Trapp, R. J. (2000). A Clarification of Vortex Breakdown and Tornadogenesis. *Monthly*
1057 *Weather Review*, 128, 888-895. https://doi.org/10.1175/1520-
1058 0493(2000)128<0888:ACOVBA>2.0.CO;2

1059 Vendrasco, E. P., Sun, J., Herdies, D. L., & Frederico de Angelis, C. (2016). Constraining a
1060 3DVAR Radar Data Assimilation System with Large-Scale Analysis to Improve Short-Range
1061 Precipitation Forecasts. *Journal of Applied Meteorology and Climatology*, 55, 673-690.
1062 https://doi.org/10.1175/JAMC-D-15-0010.1

1063 Wurman, J. (2002). The Multiple-Vortex Structure of a Tornado. *Weather and Forecasting*,
1064 17, 473-505. https://doi.org/10.1175/1520-0434(2002)017<0473:TMVSOA>2.0.CO;2

1065 Xie, Z., & Bueh, C. (2015). Different Types of Cold Vortex Circulations over Northeast
1066 China and Their Weather Impacts. *Monthly Weather Review*, 143, 845-863.
1067 https://doi.org/10.1175/MWR-D-14-00192.1

1068 Xue, M., Hu, M., & Schenkman, A. D. (2014). Numerical Prediction of the 8 May 2003
1069 Oklahoma City Tornadic Supercell and Embedded Tornado Using ARPS with the
1070 Assimilation of WSR-88D Data. *Weather and Forecasting*, 29, 39-62.
1071 https://doi.org/10.1175/waf-d-13-00029.1

1072 Xue, M., & Martin, W. J. (2006). A High-Resolution Modeling Study of the 24 May 2002
1073 Dryline Case during IHOP. Part I: Numerical Simulation and General Evolution of the
1074 Dryline and Convection. *Monthly Weather Review*, 134, 149-171.
1075 https://doi.org/10.1175/mwr3071.1

1076 Xue, M., Wang, D., Gao, J., Brewster, K., & Droegemeier, K. (2003). The Advanced
1077 Regional Prediction System (ARPS), storm-scale numerical weather prediction and data
1078 assimilation. *Meteorology and Atmospheric Physics*, 82, 139-170.
1079 https://doi.org/10.1007/s00703-001-0595-6

1080 Xue, M., Zhao, K., Wang, M., Li, Z., & Zheng, Y. (2016). Recent significant tornadoes in
1081 China. *Advances in Atmospheric Sciences*, 33, 1209-1217. https://doi.org/10.1007/s00376-
1082 016-6005-2

1083 Yokota, S., Seko, H., Kunii, M., Yamauchi, H., & Niino, H. (2016). The Tornadic Supercell
1084 on the Kanto Plain on 6 May 2012: Polarimetric Radar and Surface Data Assimilation with
1085 EnKF and Ensemble-Based Sensitivity Analysis. *Monthly Weather Review*, 144, 3133-3157.
1086 https://doi.org/10.1175/MWR-D-15-0365.1

1087 Zhang, F., Snyder, C., & Sun, J. (2004). Impacts of Initial Estimate and Observation
1088 Availability on Convective-Scale Data Assimilation with an Ensemble Kalman Filter.
1089 *Monthly Weather Review*, 132, 1238-1253. https://doi.org/10.1175/1520-
1090 0493(2004)132<1238:IOIEAO>2.0.CO;2

1091 Zhang, T., Guan, L., Zheng, Y., Chen, C., Cai, K., Li, D., et al. (2020a). Damage Survey of
1092 the 3 July 2019 Kaiyuan Tornado in Liaoning Province and Its Evolution Revealed by
1093 Disaster. *Meteorological Monthly*, 46, 603-617. https://doi.org/10.7519/j.issn.1000-
1094 0526.2020.05.002

1095 Zhang, X., Sun, J., Zheng, Y., Zhang, Y., Ma, R., Yang, X., et al. (2020b). Progress in Severe
1096 Convective Weather Forecasting in China since the 1950s. *Journal of Meteorological*
1097 *Research*, 34, 699-719. https://doi.org/10.1007/s13351-020-9146-2

1098 Zheng, Y., Lan, Y., Cao, Y., Zhang, X., Chen, C., Zhu, W., et al. (2020). Environmental
1099 Conditions, Evolution and Mechanisms of the EF4 Tornado in Kaiyuan of Liaoning Province
1100 on 3 July 2019. *Meteorological Monthly*, 46, 589-602. https://doi.org/10.7519/j.issn.1000-
1101 0526.2020.05.001

1102 Zou, H., Zhang, S., Liang, X., & Yi, X. (2018). Improved Algorithms for Removing Isolated
1103 Non-Meteorological Echoes and Ground Clutters in CINRAD. *Journal of Meteorological*
1104 *Research*, 32, 584-597. https://doi.org/10.1007/s13351-018-7176-9

1105